Building and Environment 256 (2024) 111444

Contents lists available at ScienceDirect

Building and Environment

journal homepage: www.elsevier.com/locate/buildenv

Analysis of the airflow features and ventilation efficiency of an Ultra-Clean-Air operating theatre by qDNS simulations and experimental validation

Carlos A. Duque-Daza [a,b,*], Jairo Murillo-Rincón [a,c], Andrés S. Espinosa-Moreno [a], Federico Alberini [c,b], Alessio Alexiadis [b], Diego A. Garzón-Alvarado [a], Andrew M. Thomas [d], Mark J.H. Simmons [b]

[a] GNUM Research Group, Department of Mechanical and Mechatronics Engineering, Universidad Nacional de Colombia, Carrera 30 45-03, Bogota D.C., 111321, Colombia
[b] School of Chemical Engineering, University of Birmingham, Edgbaston Campus, Birmingham, B15 2TT, United Kingdom
[c] Department of Industrial Chemistry "Toso Montanari", University of Bologna, Viale del Risorgimento 4, Bologna, 40131, Italy
[d] Royal Orthopaedic Hospital, Bristol Road South, Birmingham, B31 2AP, United Kingdom

ARTICLE INFO

Keywords:
CFD of Ultra Clean Air Operating Theatres
Indoor turbulent flow
Indoor laminar flow
Indoor airflow patterns
CFD by qDNS modelling of indoor airflow

ABSTRACT

Ultra-Clean-Air (UCA) operating theatres aim to minimise surgical instrument contamination and wound infection through high flow rates of ultra-clean air, reducing the presence of Microbe Carrying Particles (MCPs). This study investigates the airflow patterns and ventilation characteristics of a UCA operating theatre (OT) under standard ventilation system operating conditions, considering both empty and partially occupied scenarios. Utilising a precise computational model, quasi-Direct Numerical Simulations (qDNS) were conducted to delineate flow velocity profiles, energy spectra, distributions of turbulent kinetic energy, energy dissipation rate, local Kolmogorov scales, and pressure-based coherent structures. These results were also complemented by a tracer gas decay analysis following ASHRAE standard guidelines. Simulations showed that contrary to the intended laminar regime, the OT's geometry inherently fosters a predominantly turbulent airflow, sustained until evacuation through the exhaust vents, and facilitating recirculation zones irrespective of occupancy level. Notably, the occupied scenario demonstrated superior ventilation efficiency, a phenomenon attributed to enhanced kinetic energy induced by the additional obstructions. The findings underscore the critical role of UCA-OT design in mitigating MCP dissemination, highlighting the potential to augment the design to optimise airflow across a broader theatre spectrum, thereby diminishing recirculation zones and consequently reducing the propensity for Surgical Site Infections (SSIs). The study advocates for design refinements to harness the turbulent dynamics beneficially, steering towards a safer surgical environment.

1. Introduction

The concept of "operating theatres" originated from the design of rooms intended for the observation of surgical procedures by students, bearing a striking resemblance to the anatomy dissection theatres of early medical schools [1]. The advent of the 20th century brought about a paradigm shift in the design of these theatres, largely influenced by the pioneering research into bacterial infections by Louis Pasteur and Robert Koch. The first modern operating theatre, constructed by Neuber in Keil, Germany, in 1885, incorporated washable surfaces, glass and metal shelving and tables, and heat sterilisation of instruments, which were rapidly adopted worldwide [2]. Neuber also acknowledged the importance of airflow control and room geometry in minimising instrument and wound contamination, thereby reducing Surgical Site Infections (SSIs) [3]. The significance of ventilation and ambient conditions in the operating theatre in influencing the probability of SSI and postoperative complications has also been recognised [4].

The impact of airborne infection varies across different surgical disciplines. While it may be relatively insignificant in abdominal surgery, it is considered critical in orthopaedic procedures and other surgeries involving implants, such as neurosurgical shunts. The early development of joint replacement surgery witnessed an unacceptable infection

* Corresponding author at: GNUM Research Group, Department of Mechanical and Mechatronics Engineering, Universidad Nacional de Colombia, Carrera 30 45-03, Bogota D.C., 111321, Colombia.
E-mail addresses: caduqued@unal.edu.co, C.A.Duque-Daza@bham.ac.uk (C.A. Duque-Daza).

https://doi.org/10.1016/j.buildenv.2024.111444
Received 15 September 2023; Received in revised form 24 February 2024; Accepted 22 March 2024
Available online 26 March 2024

rate of up to 7% in total hip replacements [5]. Subsequent research revealed that large implants could become infected by low-grade skin bacteria, which are predominantly present on skin scales shed into the theatre environment by the surgical team [6].

1.1. Ultra Clean Air (UCA) operating theatres

In response to this challenge, Charnley collaborated with a ventilation engineer, Hugh Howorth, to develop an Ultra Clean Air (UCA) operating theatre, characterised by an engineered stream of air. They observed a decline in the infection rate as the number of air changes per hour in the theatre increased, leading to an improvement in environmental microbiology. The efficacy of UCA theatres designed by Charnley and Howorth was confirmed in a large randomised controlled clinical trial conducted in the early 1980s, and they are now standard procedure for joint replacement surgery [7]. Developments in ultra clean air rooms were not confined to the medical field. Simultaneously, engineers were devising new designs of cleanrooms for the burgeoning microelectronics industry [8–11]. These designs contributed to the development of UCA operating theatres [12]. Several international scientific organisations have since developed guidelines for operating theatres, encompassing considerations such as the filtering system and clean-air flow, positive pressure, and continuous monitoring of surgical equipment [3,13,14].

Despite advancements in surgical technique and the routine use of UCA theatres, deep infection remains a significant problem, which has not improved in recent years [15]. Real-world data on the microbiological performance of operating theatres indicates wide variability in their effectiveness [16–21]. Variations in microbiological performance are discernible in joint registry data, which exhibit inconsistent benefits of UCA theatres on infection rates [22]. The observed variability in effectiveness is likely attributable to a combination of human factors, such as intra-theatre foot traffic, and design considerations like the dimensions of the ultra-clean zone, the arrangement of surgical lights and other fixtures, and the efficacy of theatre attire. Further complexity arises from infrastructural elements such as heating, ventilation, and air conditioning (HVAC) systems [23–25]. These observations highlight substantial gaps in our understanding of UCA system performance, thus presenting opportunities for design enhancements.

1.2. Ventilation efficiency

Ventilation efficiency, as defined by Sandberg [26], refers to the ability of a ventilation system to effectively transport pollutants from their origin to the point of extraction or dilution, thus maintaining environmental pollutant levels within acceptable limits. Ventilation efficiency within confined spaces plays a pivotal role in both the design and assessment of various environments, especially those where superior air quality is paramount. In specialised settings like surgical and operating theatres, where rigorous sterilisation and infection control are essential, the importance of ventilation efficiency is amplified. Any deficiency in the design or functionality of the ventilation system may heighten the risk of infection, potentially compromising the safety of both patients and medical staff.

High-fidelity numerical simulations serve as a critical cornerstone in analysing ventilation efficiency within enclosed spaces. By harnessing numerical and computational methodologies, one can effectively model intricate air flows and pollutant behaviours within these environments, thereby facilitating the detection of design and operational shortcomings in ventilation systems, as well as the optimisation of ventilation efficiency in the interest of occupant health and safety. An array of studies, including those spearheaded by van Hooff and Blocken [27], Wang et al. [28], and Chao et al. [29], have shed light on the application of such simulation techniques in a diverse set of contexts, ranging from semi-enclosed stadiums to varying operating room configurations, and even economy-class airplane cabins. These investigations collectively underscore the transformative potential of these methodologies in deepening our comprehension of ventilation efficiency within enclosed spaces, with clear implications for enhancing the effectiveness analysis of UCA theatres.

1.3. Modelling of UCA theatres: the relevance of high fidelity simulations

In recent years, computational fluid dynamics (CFD) has gained significant prominence in the realm of ventilation in operating theatres, proving invaluable for their analysis and optimisation. Ensuring a sterile and safe environment for surgical procedures necessitates high-quality mesh simulations and high-fidelity simulations, both pivotal to optimising the design and functionality of operating theatre ventilation systems. These not only establish the ideal conditions for surgical operations but also minimise infection risk, thereby enhancing patient safety. Access to and application of high-fidelity models are indispensable for accurately predicting airflow patterns, temperature distribution, and contaminant dispersion in operating theatres [30–32]. Advancements in computational resources and numerical methods have led to marked improvements in the precision and efficiency of these simulations, allowing researchers to address complex flow problems and gain deeper insights into the underlying physics.

One vital aspect of CFD simulations in operating theatres ventilation is high-quality mesh generation, which significantly influences the accuracy and convergence of numerical solutions. Recent studies underscore the importance of employing advanced mesh generation techniques like adaptive mesh refinement, hybrid meshing, and anisotropic meshing [33]. These techniques enhance simulation accuracy by resolving critical flow features and turbulence structures, enabling more reliable predictions of air distribution patterns, temperature fields, and contaminant dispersion in the operating theatre environment [34]. An appropriately designed mesh ensures the suitable resolution and distribution of computational cells within the simulation domain, capturing essential flow features while minimising numerical errors and computational time [35]. High-resolution meshes are particularly crucial for accurately simulating turbulent flows, common in operating theatres due to complex interactions between supply air, room geometry, and medical personnel [36].

High-fidelity simulations, such as Large Eddy Simulations (LES) and Direct Numerical Simulations (DNS), are powerful tools for predicting complex flow phenomena. Recent studies attest to the advantages of high-quality mesh simulations in operating theatre ventilation system design [37,38]. For instance, Tao et al. [39] used high-quality mesh simulations to assess the effect of human-induced wake flow and particle re-dispersion and contaminant removal. The study demonstrated that higher walking speeds significantly reduce the risk of Surgical Site Infections (SSIs) by improving overall ventilation effectiveness. Similarly, Sadrizadeh et al. [40] employed high-quality mesh simulations to examine the impact of surgical staff positioning on airflow patterns and contaminant dispersion, emphasising the importance of proper personnel arrangement in minimising infection risks. High-fidelity simulations provide accurate predictions of turbulence structures and flow features, which are critical for understanding the behaviour of airborne particles and contaminants in the surgical environment. However, high-fidelity simulations often require substantial computational resources, leading to the emergence of hybrid approaches that amalgamate the strengths of both LES and Reynolds-Averaged Navier–Stokes (RANS) models [41,42]. The global Covid-19 pandemic further underscored the need for high-fidelity simulations of operating theatres and their ventilation systems. In fact, concerns about the effectiveness of existing ventilation systems in preventing the spread of infections, such as the SARS-CoV-2 virus, motivated the use of Hi-Fi simulations to investigate infection control in closed environments and aerosol and droplet dispersion in operating theatres, offering invaluable insights for the development of more effective infection control measures [43–46].

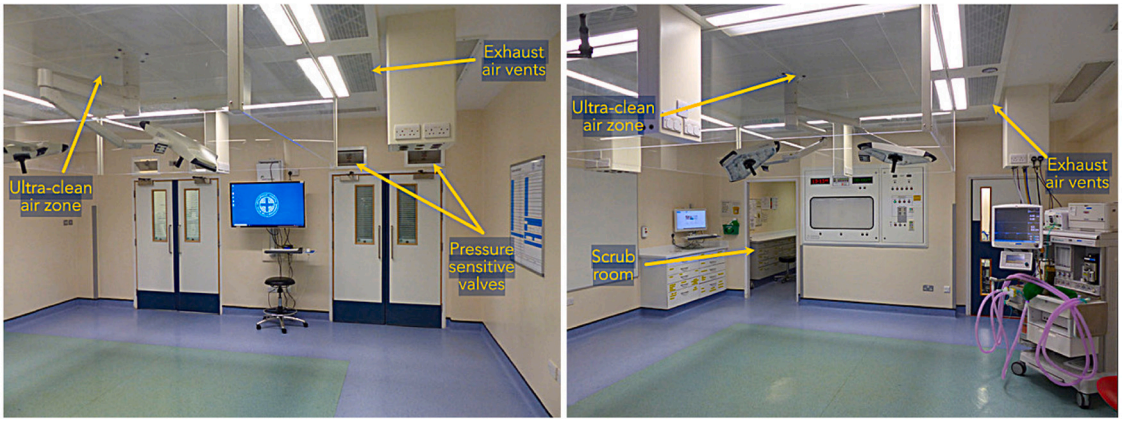

Fig. 1. Details of operating theatre 3 at ROH — Birmingham, UK. Left: Doors connecting theatre with external space. Right: Small scrub room opposite theatre's doors.

Accordingly, it seems clear that computational simulations, primarily reliant on high-quality meshes, are extremely helpful in studying airflow and ventilation in operating theatres. These simulations offer accurate insights into complex flow phenomena, ensuring optimal surgical conditions. After the global pandemic in 2020, these techniques have become vital for enhancing infection control measures. As mesh generation techniques and turbulence models advance, along with increasing computational resources, we expect further progress in ventilation system design.

1.4. Summary, novelty, and roadmap

According to the previous arguments, the study of flow dynamics in operating theatres is critically important, particularly for understanding the efficiency of ultra-clean air systems, the behaviour of biological entities, and the impact of room layout. Conventional instruments like hot-wire and vane anemometers, while useful for routine assessments, fall short in accurately delineating complex airflow patterns. Ultrasound-based anemometers, despite their enhanced accuracy, are seldom used in operating theatres, possibly due to their need for correction in high-frequency and large-wavenumber scenarios. Regardless, these devices provide limited comprehensive airflow patterns insights, requiring expensive and extensive observations.

The potential of CFD models as cost-effective tools for operating theatres analysis and design has been documented in [47]. However, traditional CFD studies in operating theatres often adopt laminar flow assumption, potentially underestimating localised turbulence [18,48]. In fact, the efficacy of Computational Fluid Dynamics (CFD) in these analyses hinges on computational robustness and the accuracy of results across various spatial and temporal scales. While simpler laminar models with low-resolution meshes, or advanced turbulence models like Large Eddy Simulation (LES), are effective within their specific flow regimes, their applicability is limited by the inability to predict these regimes a priori in complex environments like operating theatres. Here, quasi-Direct Numerical Simulation (qDNS) emerges as a solution, offering high-resolution capabilities essential for analysing multi-regime flow phenomena in such settings.

In the present work, a robust Computational Fluid Dynamics (CFD) model for an Ultra Clean Air (UCA) operating theatre is developed employing a quasi-Direct Numerical Simulation (qDNS) approach with a highly-to-medium resolved mesh. The primary objective is to elucidate factors influencing theatre performance, including the intricate relationship between room geometry, air circulation, and ventilation dynamics. These elements are critical for optimising operating theatre (OT) designs, particularly for daily operational considerations.

Our approach involved validating the CFD model using ultrasound-based anemometer measurements, enabling a detailed analysis of a specific UCA theatre. The adopted modelling process was instrumental in enhancing our understanding of the transition to turbulent regimes and localised dissipation phenomena within the theatre. Such phenomena are of paramount importance in environments where stringent asepsis is required. The insights gained from our qDNS-based flow simulations extend beyond mere theoretical understanding; they are pivotal in refining numerical models to more accurately reflect real-world conditions. This includes exploring aspects like gas evacuation in enclosed spaces and the identification of stagnant air zones. Consequently, our findings contribute significantly to the advancement of aseptic conditions in these critical environments, laying a foundation for future enhancements in OT design and performance.

The present manuscript is organised as follows: in Section 2 a detailed description of the targeted operating theatre is presented, as well as some of the characteristics of the Ultra Clean Air (UCA) ventilation system currently working in the selected theatre. In Section 3 the experimental and numerical methodologies employed in this work are described, and the construction of the computational model is discussed in more detail. The validation results are presented and discussed in Section 4 where special attention is given to velocity profiles and energy spectrum. In Section 5 the main body of results is presented and discussed, including flow patterns, turbulent kinetic energy, dissipation, and ventilation efficiency. Finally, in Section 6, conclusions are drawn and presented, along with a short discussion about the possible future work and applications of the proposed methodology.

2. Details of the Ultra Clean Air Operating Theatre (UCA-OT)

The operating theatre number three (3) of the Royal Orthopaedic Hospital in Birmingham (UK) was selected as target environment for the present study. This operating theatre is composed of multiple interconnected spaces, although for simplicity only two were considered for the present study: the main operating room, shown in both pictures of Fig. 1, where the actual surgical procedures are performed, and another smaller room, commonly referred to as "scrub room", which is permanently open to the main operating theatre as shown in the right picture of Fig. 1, therefore conforming in fact a single environmental space. The main theatre is also connected to other spaces through two doors, opposite to the scrub room, which usually remain closed during the procedures, therefore acting as a wall that blocks the airflow from within the operating theatre (see left pinture in Fig. 1). In this work we will refer to the main operating theatre as "the main room", or simply "the operating theatre". When needed, we will refer to the main operating theatre together with the small scrub room as the "enlarged theatre".

The operating theatre presents an ultra-clean air (UCA) zone produced by an Howorth Exflow 90 system coupled with a canopy of partial walls (Howorth Exflow 90, Howorth Airtech, Bolton, UK), through which recirculated HEPA filtered clean air is injected into the operating

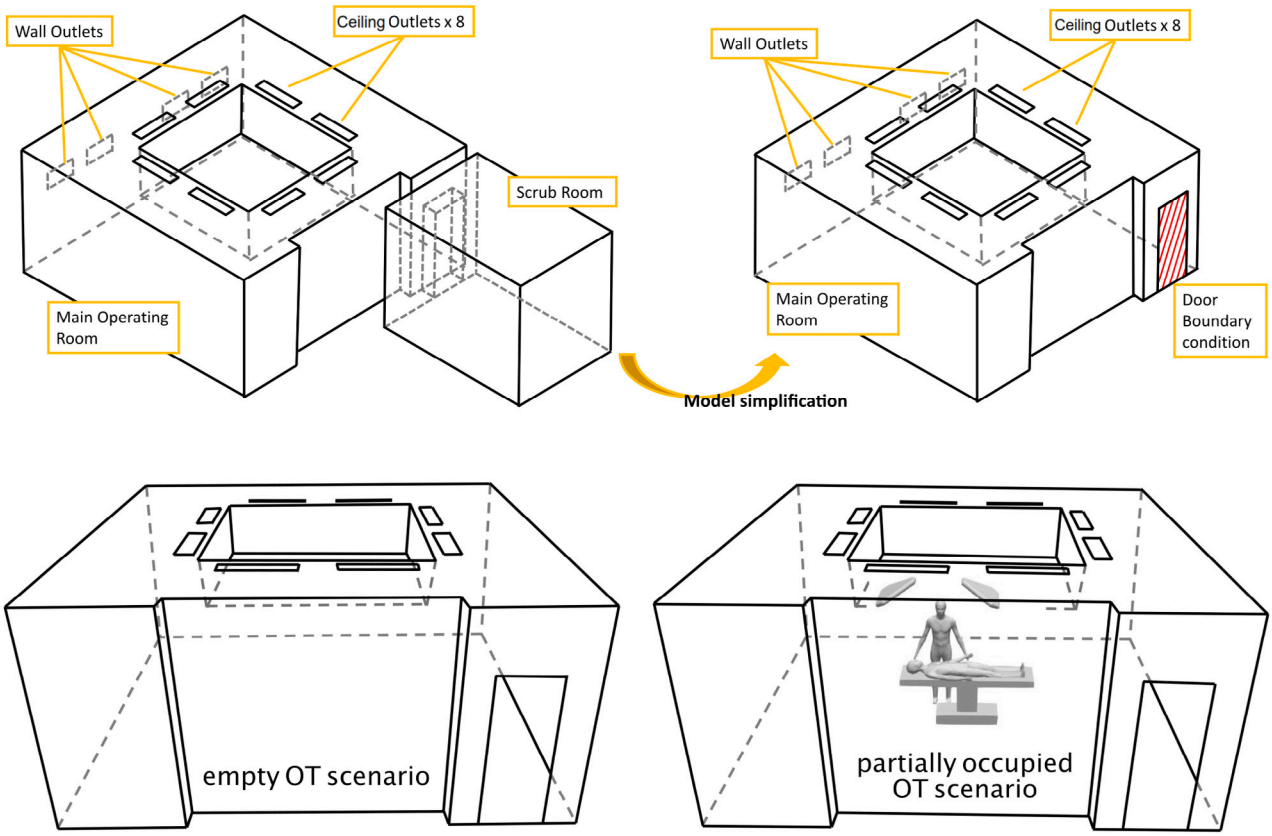

Fig. 2. Top row: computational domain simplification, scrub room replaced by a post-hoc adapted boundary condition. Bottom row: computational domains for the empty operating theatre scenario (left), and for the partially occupied scenario right.

theatre. The ultra-clean zone, located in the middle of the operating theatre, measures 2.8 m × 2.8 m. The clean zone is compliant with UK Health Technical Memorandum HTM 03–1, which specifies a minimum downflow of ultraclean air of 0.2 m/s at 1 m above ground level, and 0.38 m/s at 2 m above ground level within the UCA. The main operating theatre has a total area of 41 m^2 (6.06 m × 6.76 m). The theatre is of a slightly older design, so although the UCA zone is HTM 03-1 compliant, the floor size of the whole room is smaller than current requirements.

The Howorth Exflow 90 system is intended to act also as a laminar air flow (LAF) system by enforcing a mainly vertically directed airflow in the central part of the theatre. In fact, as shown later, this system produces a distinct global "inverted trumpet" airflow path that initially directs the air vertically downwards towards the operating area and then up towards a set of exhaust air vents located in the ceiling, adjacent to the UCA zone just outside the canopy (see left Fig. 1), from where the air is recirculated. There is a net input of air into the operating theatre from an air handling unit, which is essential to provide fresh air for the staff to breath, and to dilute anaesthetic gases. The number of air changes in the room is specified in guidance. The net input of air into the room is also exhausted either through the doors, when they are open, or through pressure sensitive mechanical valves above the doors when the doors are closed. The UCA canopy filters and recirculates the air in the room, to produce a specified downflow in the UCA zone.

The Howorth LAF system is usually set to achieve an internal temperature of around 20 °C, at its maximum airflow capacity of 2979 L/s. Although system manufacturer's data was available, the actual performance of the system was also checked by using four pitot traverses to measure the input to the system, and the recirculated air was checked with a balometer. The system was found to be closely performing in accordance to the manufacturer's specification: the net input of fresh air from the air handling unit was found to be 931 L/s, whereas the recirculated air was rated at about 2167 L/s, meaning that the total canopy airflow was around 3098 L/s. For the experiments in the present work, the airflow system was set to achieve an internal temperature of 20 °C. This condition was also used to define the thermophysical characteristics of the flow in the numerical simulations.

Aiming to improve the performance of the computational model employed in the production simulations, the scrub room was omitted, and the effect of its presence was modelled by post-hoc fitted boundary condition using the experimental data and a set of preliminary simulations. This domain modification allowed for a better mesh density in the main operating theatre. A schematic representation of this domain simplification is illustrated in the top of Fig. 2.

The goal of this study was to analyse the flow patterns and ventilation properties of an empty operating theatre and compare them with a lightly occupied scenario, emulating simplified surgical conditions. Therefore, we evaluated the theatre's performance using two spatial configurations: an empty theatre and a theatre occupied with two lamps, an operating table, a patient, and a standing surgeon. These configurations are depicted in the bottom of Fig. 2. It is important to clarify that the chosen layout for the occupied theatre scenario does not represent all possible occupied spaces. Given the diversity of surgical procedures and, consequently, operating theatre layouts, it is difficult to declare one layout as universally relevant or representative. The myriad of possibilities precludes a direct comparison or the designation of a single layout as emblematic of the majority. Regardless, a minimal occupation example scenario serves as a legitimate basis for investigating the impact of obstacles within the theatre, regardless of the degree of occupancy. This approach is underpinned on the hypothesis that some observable effects in a simplified case are likely to indicate similar or more pronounced effects in more complex or realistic scenarios.

3. Methodology

The elucidation of flow dynamics and ventilation efficiency in the investigated operating theatre was carried out by means of a comprehensive experimental characterisation combined with high-fidelity numerical simulations. The experimental investigation served a dual purpose: first, it provided preliminary information and data on flow patterns, thus facilitating the simplification of the computational domain. Subsequently, it functioned as a repository of tailor-made validation data for the computational model that was implemented and employed throughout this study. Furthermore, the current investigation conducted a comparative analysis of the intricacies of the operating theatre's fluid dynamics, encompassing turbulence and ventilation attributes, between the unoccupied and minimally occupied scenarios. To facilitate this comparison, the computational model was designed to incorporate two distinct computational domains for the operating theatre: one representing an unoccupied state and the other simulating a scenario with internal obstructions. The following sections systematically detail the experimental methodology and the computational model used to numerically simulate the scenarios described.

3.1. Experimental set-up and procedure

We employed a WindMaster 3D Sonic Anemometer (Gill Instruments Limited, Lymington, UK) to capture the complex flow dynamics within the operating theatre. This instrument, equipped with three ultrasound probes and receivers, one for each velocity component, can sample at a frequency of 32 Hz. It is typically used for measuring air turbulence in various contexts such as around buildings, turbine sites, and ventilation systems. Its high sampling frequency enhances its sensitivity, making it ideal for measuring wind speeds at close ranges, as anticipated under the Howorth Exflow 90.

The anemometer was securely mounted on a pole attached to a tripod, providing a stable base with adjustable height. We collected measurements at various locations across a theatre's mid-plane, from the canopy's centre and extending to the wall opposite the scrub room entrance. A total of 72 locations were probed, arranged in a two-dimensional Cartesian grid. The probes were positioned at $x = 0.06, 0.56, 1.06, 1.31, 1.51, 1.76, 2.01, 2.26,$ and 2.6 m, where x represents the horizontal distance from the theatre's centre to the wall opposite the scrub room. Vertically, probes were placed at heights $z = 0.48, 0.75, 1.00, 1.50, 1.75, 2.00, 2.25,$ and 2.45 m from the floor. The location of these sampling probes is illustrated in Fig. 5(c).

Before each measurement, we allowed a stabilisation period of 10 to 20 s to normalise the flow disrupted by equipment and personnel movement. Subsequently, measurements were taken for a minimum of 30 s, ensuring a data sample of 1000 points for a reliable steady-state velocity average. This velocity data was processed to construct a comprehensive airflow field within the operating theatre, also providing the necessary validation data for our computational model.

3.2. Mathematical model

Airflow and ventilation dynamics within an Ultra Clean Air (UCA) operating theatre occur at low Reynolds and Mach numbers. Thus, in our numerical simulations for both vacant and occupied scenarios, we assumed incompressible, isothermal airflow. We employed the conservation of mass and momentum equations as the mathematical model to represent these flow conditions, expressed as:

$$\nabla \cdot \mathbf{U} = 0 \tag{1}$$

for the mass conservation, and as:

$$\frac{\partial \mathbf{U}}{\partial t} + \mathbf{U} \cdot \nabla \mathbf{U} = -\nabla p + \nu \nabla^2 \mathbf{U} \tag{2}$$

for the principle of conservation of momentum, where $\mathbf{U}$ is the fluid velocity field, p is the pressure normalised by the density and ν is the kinematic viscosity of the fluid. For a transient, incompressible, three-dimensional flow, Eq. (2) is the most common mathematical model, with Eq. (1) usually taken as a constraint that the computational model must meet to provide for flow incompressibility.

3.3. Computational model

The numerical experiments were conducted using an Eulerian framework and the finite volume method for spatial discretisation. We utilised OpenFOAM (OF), an open-source CFD toolbox, for model development. OF offers a balance between readily available simulation tools and the flexibility of open-source code, enabling efficient customisation for specific research. We used one of OF's standard solvers for turbulent incompressible flow, *pimpleFoam*, for all experiments. This solver allows for turbulence modelling and uses PIMPLE technique for pressure–velocity coupling, a more stable version of the standard PISO method [49,50].

3.3.1. Computational mesh

High-fidelity simulations were the primary focus of this study, necessitating meticulous mesh discretisation of the model's domain. Rather than using a turbulence model, we employed dense computational meshes and second-order numerical schemes to capture key flow patterns. This approach aligns with quasi-Direct Numerical Simulation (qDNS) or unresolved Direct Numerical Simulation (uDNS) methodologies [51], effectively capturing the main flow characteristics, including turbulence, within the operating theatre.

The qDNS methodology represents a hybrid modelling approach, effectively bridging the gap between traditional Direct Numerical Simulation (DNS) and conventional Large Eddy Simulation (LES). Its primary objective is to resolve a substantial portion of the turbulent spectrum, thereby capturing more of the inertial subrange of turbulence, without necessitating the full resolution of all scales of motion [52,53]. This approach involves a strategic balance of grid and scale management, employing a mesh resolution that is finer than that typically used in LES, yet coarser than in DNS. Notably, the qDNS methodology minimises or entirely omits turbulence modelling, eschewing subgrid-scale (SGS) modelling typical of LES. Instead, it relies on mesh density to capture the essential physics of turbulent flows. This technique is particularly advantageous in scenarios where small-scale turbulence details are crucial, but the computational demands of full DNS are prohibitive [54]. The efficiency of qDNS in capturing critical turbulent structures makes it an ideal choice for detailed analysis of complex flow patterns [55,56]. In our study, we have exclusively depended on mesh density, deliberately avoiding explicit SGS modelling. We have instead utilised the inherent numerical diffusion of our chosen numerical methods. This approach aligns with findings that numerical dissipation can effectively mirror the dissipative effects of explicit SGS modelling in LES, as explored in depth by [55,57].

Regarding turbulence capture, our computational mesh was designed based on initial estimates of relevant length scales, particularly the Kolmogorov length scale. This scale, denoted as η_κ, is a key parameter in turbulence theory, representing the smallest spatial scale of turbulent eddies, and defined as $\eta_\kappa \approx L/\mathrm{Re}^{3/4}$, where L is a large representative flow length scale, and Re a related Reynolds number. A global value for η was computed using the boundary layer thickness (δ) of the flow over the canopy as the largest spatial scale and the Reynolds number based on δ (Re_δ), the inlet flow rate and the air properties at 20 °C. With the boundary layer thickness estimated as $\delta \approx 0.03$ m for the inlet dimensions and the provided inlet flow rate (2.98 m^3/s), and $Re_\delta \approx 700$, a general Kolmogorov scale was initially estimated as $\eta_\kappa \approx 2.0 \times 10^{-4}$ m. The computational model utilised a mesh exceeding 10 million cells, yielding an average cell-based length of $L_\Delta \approx 5.1 \times 10^{-3}$, m. This configuration, which aligns with the quasi-Direct Numerical Simulation (qDNS) approach, ensured a cell-based length-to-Kolmogorov ratio within the acceptable range for qDNS

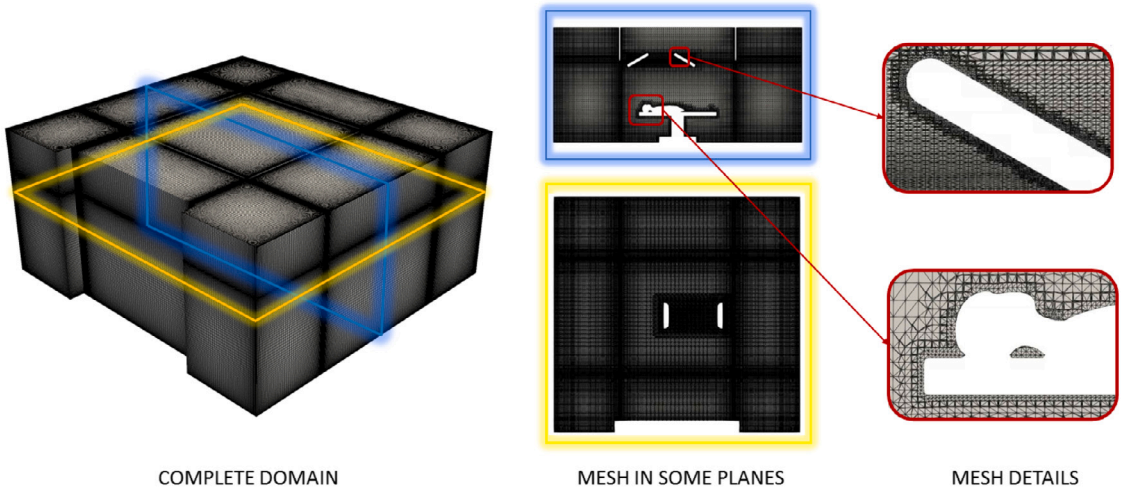

Fig. 3. Computational mesh. Left: near-canopy refinement influence over the OT domain mesh. Centre: details at horizontal (yellow) and vertical (blue) planes in the occupied OT scenario. Right: details of mesh refinement near lamp and head of patient boundaries, treated as solid non-slip walls. (For interpretation of the references to colour in this figure legend, the reader is referred to the web version of this article.)

resolution. Additionally, our mesh configurations were refined near all non-slip boundaries, maintaining an average cell size of $L_{\Delta}^{+} \approx 2$. General overview of the computational, as well as mesh details for the occupied room scenario are illustrated in Fig. 3.

3.3.2. Boundary conditions

In both scenarios studied, the operating theatre walls were considered impermeable boundaries enforcing a no-slip condition. This was also applied to all obstructions in the occupied OT scenario. In accordance with the physical layout of the operating theatre, twelve flow outlets were established: four on the wall opposite the scrub room and eight on the ceiling, located adjacent to the canopy walls. In line with the operating theatre's design, a central UCA flow inlet was set up in the ceiling, as depicted in the schematic layout previously presented in Fig. 1. The UCA system generates a flow with a deficiency near the inlet borders, likely due to boundary layer effects. To capture this behaviour, a synthetic two-dimensional velocity profile was used as a Dirichlet condition at the ultraclean inlet, defined by a Gaussian function given by Eq. (3). Here, x and y denote the position coordinates in the plane of the inlet, with the origin at the centre of the UCA inlet. The adjustment coefficients α and β were set to -0.45 and 1.92, respectively, to maintain an inlet flow rate of approximately 2.98 m^3/s, as per specifications.

$$U = \alpha \exp\left[-\frac{x^2 + y^2}{2\beta^2}\right] \tag{3}$$

In this study, the scrub room was substituted with a calibrated boundary condition to mimic its impact on the operating theatre's airflow, as shown in Fig. 2. Precursor simulations of the entire theatre were conducted, supplemented by various calibrated boundary conditions. Two boundary conditions, a flow regulated outlet (FRO) and a pressure outlet (PO), were evaluated for their ability to accurately represent the flow behaviour, as depicted in Figs. 4(a) and 4(b). Upon comparing the flow rates at the outlets for each boundary condition, the FRO condition was found to better replicate the precursor simulation including the scrub room, as clearly observed in Fig. 4(b). Hence, the FRO condition was selected for the production simulations in this study. This approach aligns with the methodology of similar studies where preliminary simulations are used to adjust boundary conditions (see García et al. [58]).

3.3.3. Grid independence analysis (GIA)

As part of the preliminary exploration to verify spatial and temporal resolution parameters, as well as computational times, we conducted a Grid Independence Analysis (GIA) in line with the guidelines of Richardson's extrapolation outlined in Celik et al. [59]. We employed three fully structured grids, beginning with the coarsest grid comprising 2.27 million cells. The subsequent two meshes were refined by reducing the average cell size (h) by a factor of 1.3. To this end, we employed as average cell size h the cube root of the average cell volume. This process resulted in an intermediate mesh of 5.06 million cells and a finest mesh of 10.39 million cells. To assess the performance across different cases, we calculated the average inlet pressure as an indicator of the energy consumption required to maintain airflow within the system, alongside the volume integral of the turbulent kinetic energy across the entire domain. For the average pressure at the inlet, we noted an extrapolated relative error of 0.95% compared to the value obtained with the finest mesh, and a Grid Convergence Index (GCI) of 1.18%. In contrast, for the turbulent kinetic energy, an extrapolated relative error of 2.28% and a GCI of 2.92% were observed. Figs. 4(c) and 4(d) illustrates the predicted values as a function of the average cell size normalised using the value from the finest mesh, h^* (with a value of 1 corresponding to the finest mesh). Additionally, the predicted value using Richardson extrapolation is depicted using dashed lines.

3.4. Ventilation efficiency: tracer gas decay set-up

In assessing ventilation efficiency, we implemented a tracer gas decay scenario, using carbon dioxide (CO_2) as the trace pollutant in the Ultra Clean Air (UCA) environment. As per various studies, concentrations below 1000 [PPM] are considered acceptable for human exposure [28,60]. In line with research by Chung and Hsu [61], Wang et al. [28] and Wu et al. [62], an average concentration of 350–400 [PPM] is typical for enclosed environments under normal conditions. Meanwhile, studies by Chao et al. [29] and Regard et al. [63] adopt the decay method which seeks a condition where the average concentration approaches 0 [PPM]. In other research works focusing on tracer gas decay in enclosed environments, such as the study by van Hooff and Blocken [27] and the operating room investigation by Wang et al. [28], initial concentrations typically span from 1500 to 2000 [PPM]. These values are dependent on the detection capabilities of the sensors employed in experimental measurements. In alignment with these

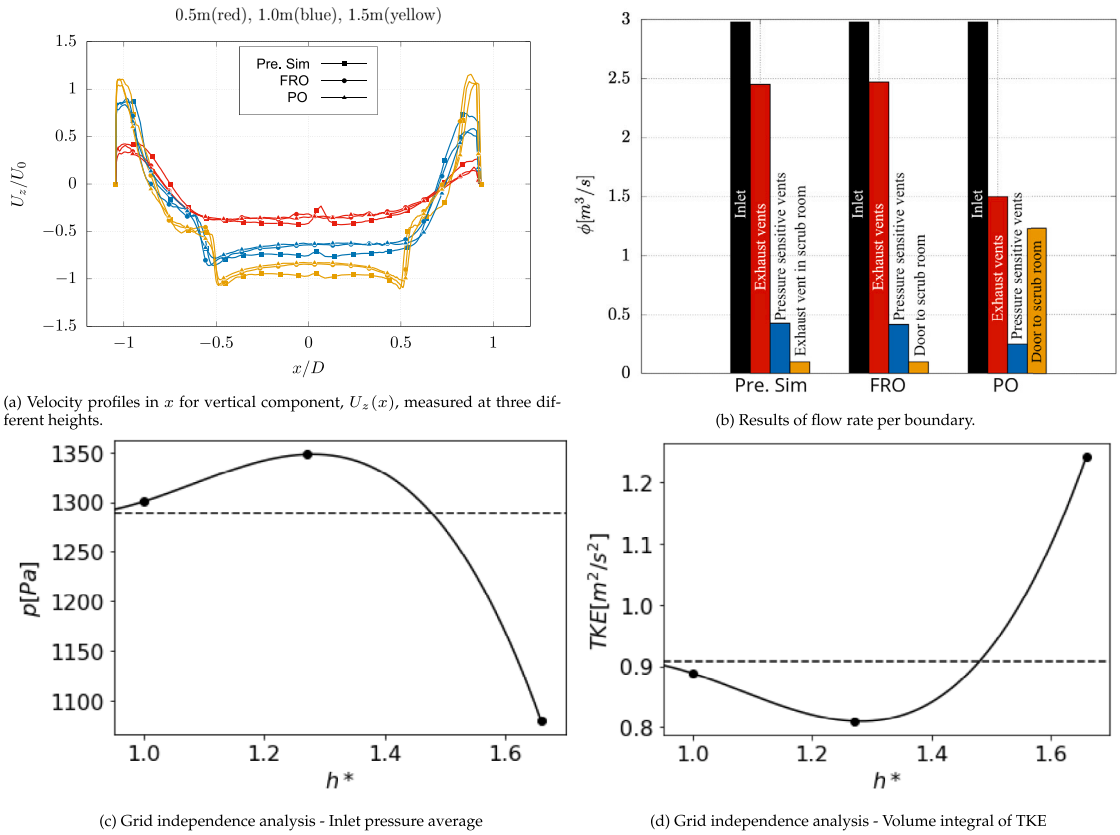

(a) Velocity profiles in x for vertical component, $U_z(x)$, measured at three different heights.

(b) Results of flow rate per boundary.

(c) Grid independence analysis - Inlet pressure average

(d) Grid independence analysis - Volume integral of TKE

Fig. 4. Preliminary analysis of computational model settings and performance. **Top row:** Comparative evaluation of velocity profiles 4(a), and Volumetric flow rates 4(b) obtained a precursor simulation incorporating the scrub room, and simulations employing a Flow Rate Outlet (FRO) and a Pressure Outlet (PO) boundary conditions. **Bottom row:** Results of GIA using average inlet pressure 4(c), and volume integral of turbulent kinetic energy 4(d), predicted using different resolution of the spatial discretisation and compared with the Richardson extrapolated value. (For interpretation of the references to colour in this figure legend, the reader is referred to the web version of this article.)

findings, the initial conditions for the numerical experiments in this study were established at an initial peak concentration of 1500 [PPM]. Simultaneously, a consistent input concentration of 400 [PPM] was maintained at the inlet. The ventilation efficiency was assessed under conditions of fully developed flow, initiating the analysis of gas decay only after a steady-state flow had been achieved in each simulation.

4. Model validation

The validation of our computational model was conducted through a comprehensive analysis of velocity behaviour, airflow patterns, and power spectra, comparing these results with experimental measurements taken at various selected locations. The agreement between our computational model and the experimental measurements is illustrated in Figs. 5(a) and 5(b), where the time-averaged and standard deviation of spatial velocity profiles are compared. These profiles were probed at horizontal lines extending from the centre of the operating theatre towards the north wall. Profiles have been normalised using U_0, the maximum inlet velocity, while the horizontal axis has been scaled using the length of the edge of the squared inlet at the ceiling, D. The airflow pattern and the reference probes grid are depicted in Fig. 5(c).

Figs. 5(a) and 5(b) demonstrate that our computational model successfully captures the spatial trends of the flow velocity measured experimentally at different heights z. While some discrepancies are present, particularly for $z = 0.45$ m and $z = 2.0$ m, the computational model's values fall within the expected experimental observations for most of the monitored locations. For instance, the velocity profiles predicted by our computational model are bounded by the standard deviations of the experimental readings at different heights.

Our validation process also entailed a post-processing of the raw experimental data for the correction of the flow velocity component signals produced by sound anemometers, following the approach developed by Nakai et al. [64]. Subsequently, an analysis based on the corrected flow velocity magnitudes was performed. The initial step involves employing an iterative algorithm to adjust each flow velocity field component, effectively minimising errors predominantly associated with the anemometer's angle of attack. This necessity stems from documented evidence by several authors that the angle of attack and the anemometer body significantly influence the surrounding flow and distort the recorded data [65–70]. Several studies (Peña et al. [66], Dyer et al. [67], Hogstrom et al. [68]) have specifically addressed the development of corrections to refine both experimental and numerical approximations, aiming to mitigate errors arising from the aforementioned disturbances. The algorithm proposed by Nakai et al. [64], and adopted in the present work, allowed us to make this data correction for the Solent WindMaster Pro anemometer used in our experiments (Gill Instruments, Lymington, UK).

Once each flow velocity component had been corrected, time-evolution series of the velocity magnitude were constructed based on the newly corrected velocity components. The validation analysis was performed for all the data obtained (72 probes), although for a focused analysis we selected three strategic locations of the experimental setup, using the anemometer readings at these locations for visual presentation of results. These locations include the A1 sensor in the upper left corner, the F4 sensor in a central position and the I3 sensor near the ground, following designations presented in Fig. 5(c). This selection covers the essential flow regimes of relevance to our research objectives.

Results of the aforementioned procedure are presented in Fig. 6. Particularly, the three images at the top of this figure show the corrected experimental velocity magnitudes for the three probes locations identified above, and the results from our numerical experiments. It can

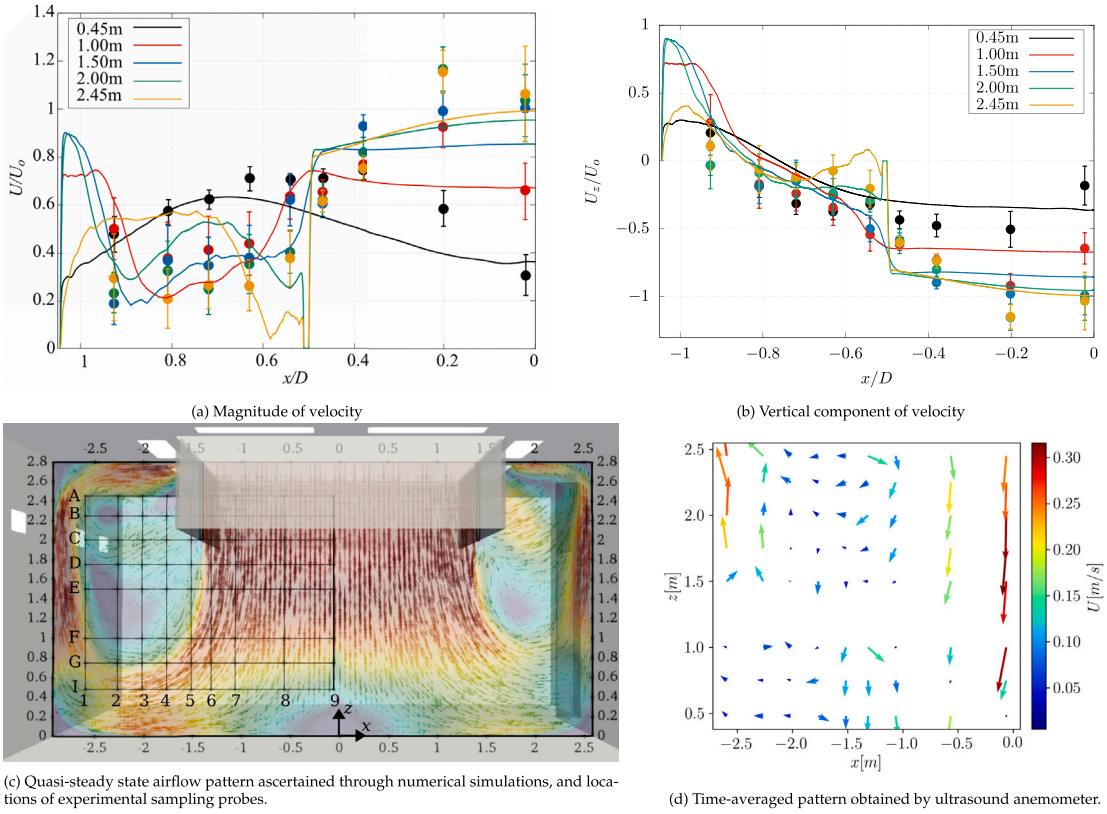

(a) Magnitude of velocity

(b) Vertical component of velocity

(c) Quasi-steady state airflow pattern ascertained through numerical simulations, and locations of experimental sampling probes.

(d) Time-averaged pattern obtained by ultrasound anemometer.

Fig. 5. (a) Velocity magnitude profiles; (b) velocity vertical component profiles; (c) Overview of airflow pattern obtained by numerical experiments and locations of experimental sampling points; (d) Airflow pattern inside the operating theatre; Values obtained and measured at different heights: black $z = 0.45$ m; red $z = 1.0$ m; blue $z = 1.5$ m; green $z = 2.0$ m; and yellow $z = 2.45$ m. (•): Experimental measurement; (–): Computational result. Standard deviation indicated by "error" bars. (For interpretation of the references to colour in this figure legend, the reader is referred to the web version of this article.)

be seen how the numerical simulation faithfully captures the trends and velocity magnitudes. Some of the flow velocity components exhibited a highly fluctuating behaviour, consistent with our experimental observations, specially at locations outside the region of injection of the Ultra Clean Air inlet (probes A1 and F4). The results from our computational model lie mostly within an error of ≈5% of the experimental observations. This error percentage was obtained by comparing the time-averaged numerical results with the corresponding experimental measurements. To further refine our comparison, we calculated the standard deviation of the experimental results, illustrated as a grey band in Fig. 6, representing ±2 standard deviations from the experimental time average. This visualisation confirms that the numerical simulation data predominantly aligns within the experimental data's range after post-processing.

Despite the observed differences in the comparative curves presented in Fig. 6, it is evident that the primary trends of the phenomenon have been successfully captured, even the fluctuating behaviour observed in our numerical results that could be attributed to the presence of laminar periodic structures or the turbulent nature of the flow, depending on the region of analysis. Notably, while the flow appears quasi-laminar within the Ultra-clean zone directly beneath the ceiling inlet, it is largely turbulent throughout the operating theatre. Our analysis revealed a more stable flow in the centre of the operating theatre, as shown for probe I3, compared to the outer regions illustrated by results at probes A1 and F4.

To further investigate the presence of turbulence and validate the consistency between numerical and experimental results, we computed the power spectra of the flow velocity time series. The results can be seen in the middle row of Fig. 6. Here it is observed again the closeness between the numerical and experimental results, especially with regard to the slope of the turbulence cascade. According to the spectra obtained for most of the locations analysed, our computational model successfully captured the trends and amplitudes of the power spectra from the experimental readings at most examined probes. This finding was consistently observed at many of other locations in the operating theatre. The most striking observation is the well-captured trends across the full range of frequencies, regardless of location. However, discrepancies in the amplitudes of velocity signals were observed, especially at high frequencies. The power spectra obtained indicate a turbulent behaviour at most locations outside the UCA zone, as the spectra resemble the turbulent energy cascade, at least up to the largest scale of the inertial range. This is far from the assumed general laminar behaviour in the theatre.

Finally, the velocity magnitudes time series and power spectra were coupled with a correlation analysis between numerical and experimental readings, shown in the bottom row of Fig. 6 for the three selected probes. This technique offers insights into the relationship between two signal sets. This approach, validated by Derrick and Thomas [71], Keane and Adrian [72] and Brito et al. [73], facilitates a nuanced understanding of signal associations, revealing a significant correlation between our experimental and numerical data. The bottom plots of Fig. 6 highlight this correlation, with all curves exhibiting positive values, indicating a consistent relationship between the behaviours of both data sets.

These findings allow us to confirm that the computational model demonstrated a high degree of agreement with experimental measurements, particularly in capturing the spatial trends and temporal evolution of flow velocity in the operating theatre. While some discrepancies exist, they are largely within the expected range of experimental observations, thereby validating the effectiveness of our model in simulating the complex fluid dynamics of this environment. It is also clear that although the dissipative range is not appropriately captured, there

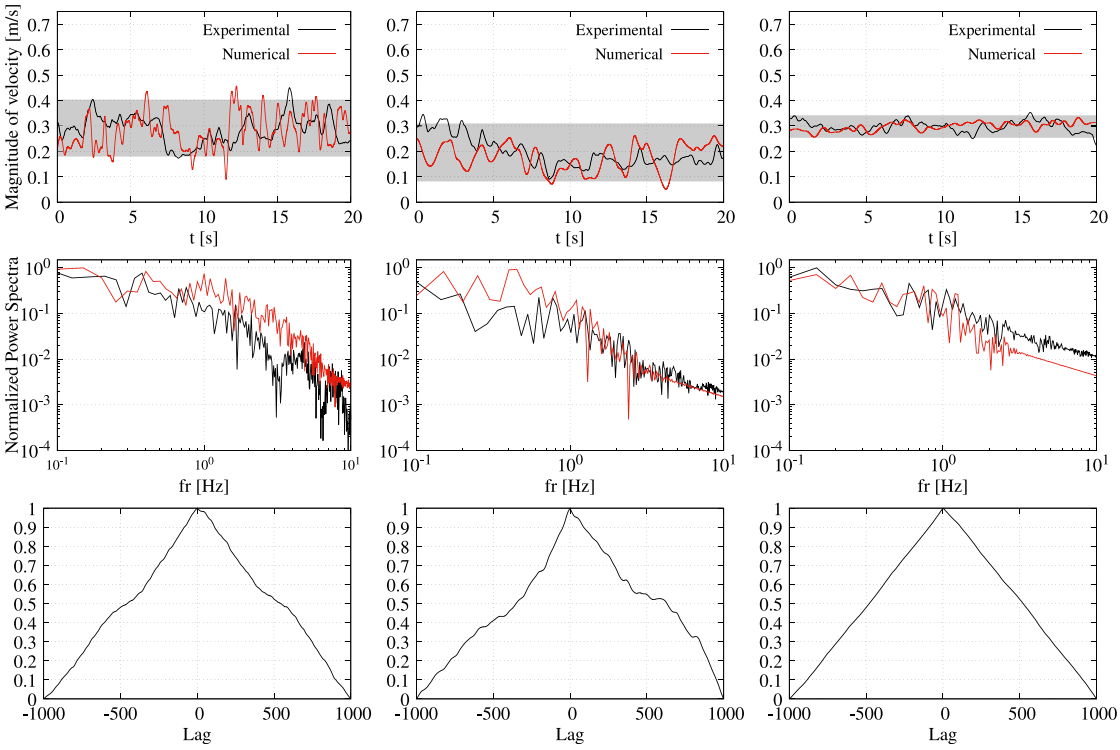

Fig. 6. Comparison of the time series for the probes A1 (left column), F4 (middle column), and I3 (right column). Top row: time signals of velocity magnitude; Middle row: power spectra of time signals; Bottom row: Cross-correlation of experimental and numerical signals. (For interpretation of the references to colour in this figure legend, the reader is referred to the web version of this article.)

is a clear close correlation between the experimental measurements and the simulations, in some locations even at the high frequencies related to the dissipation region of the turbulent energy cascade.

5. Results and discussion

A detailed investigation of airflow dynamics was undertaken in Operating Theatre No. 3 at the Royal Orthopaedic Hospital in Birmingham, UK, under two distinct scenarios: an unoccupied and a partially occupied theatre. The unoccupied condition also functioned as a validation case, mirroring the experimental test parameters (refer to Section 4). For both scenarios the airflow attributes were meticulously scrutinised, including velocity profiles, pressure-based structures, dissipation rate, and turbulent kinetic energy (TKE) distributions. Additionally, a discussion concerning the suitability of the chosen mesh quality for our model is also incorporated.

5.1. Flow patterns: velocity and pressure iso-surfaces

Airflow patterns within the Ultra Clean Air (UCA) operating theatre were meticulously analysed at various planes, both horizontally and vertically. Two specific horizontal planes, designated as Plane 1 and Plane 2, were strategically positioned at elevations of $z = 1.7$ m and 1.1 m, respectively. These elevations were chosen in accordance with the ASHRAE standard recommendations for tracer gas method measurements [74], aligning with the breathing heights of both standing and seated individuals. The examination of these horizontal planes facilitated a detailed investigation into the velocity and pressure distributions within the theatre, and allowed to provide insights into its ventilation characteristics.

Contour plots of the time-averaged flow velocity magnitude for both empty and occupied cases are depicted in Fig. 7. These plots elucidate a pronounced disparity in the velocity gradient between the central Ultra Clean Air (UCA) zone and the peripheral region of the theatre. Specifically, in the central region, the velocity gradient diminishes, as manifested by the widening distance between contour lines. In contrast, the outer zone exhibits a more acute velocity gradient, as demonstrated by the proximity of contour lines, particularly near walls and the boundary of the clean zone.

These regions of higher gradient may imply the emergence of confined recirculation zones and localised wall-jet effects. The wall-jet effects are characterised by a jet of air impinging on the wall and spreading laterally along it. This creates a thin, high-velocity layer adjacent to the wall, phenomenon leading to complex flow patterns, including turbulence and enhanced mixing. This pattern is particularly pronounced in areas where the airflow interacts with structural features, such as corners or protrusions, leading to localised acceleration of the flow and potential formation of secondary vortices. This is the flow condition observed in the OT, particularly pronounced on the boundary with the scrub room and the wall opposite featuring the four wall outlets illustrated in Fig. 1.

The contour plots in **A** and **B** of Fig. 7, corresponding to the empty case at Plane 1 and Plane 2, respectively, elucidate these patterns for the unoccupied operating theatre (OT) scenario. The velocity gradient appears fairly uniform across the theatre's central region but becomes accentuated near the walls and corners of the outer region, where higher velocity gradients are anticipated. This pattern largely persists at lower elevations, as illustrated by the contour plot at Plane 2, primarily due to the absence of internal obstructions. Nevertheless, the differentiation between the patterns in the central UCA and the outer regions becomes more conspicuous at Plane 2, likely attributable to the additional wall effects induced or amplified by the theatre's floor, including the wall-jet phenomena described above.

Another noteworthy observation from the examination of the horizontal planes is the emergence of distinct low-velocity regions or bulges. These are uniformly distributed in the outer region surrounding the central UCA zone, and their intensity amplifies at lower elevations. The pronounced variation in velocity within the outer region at these

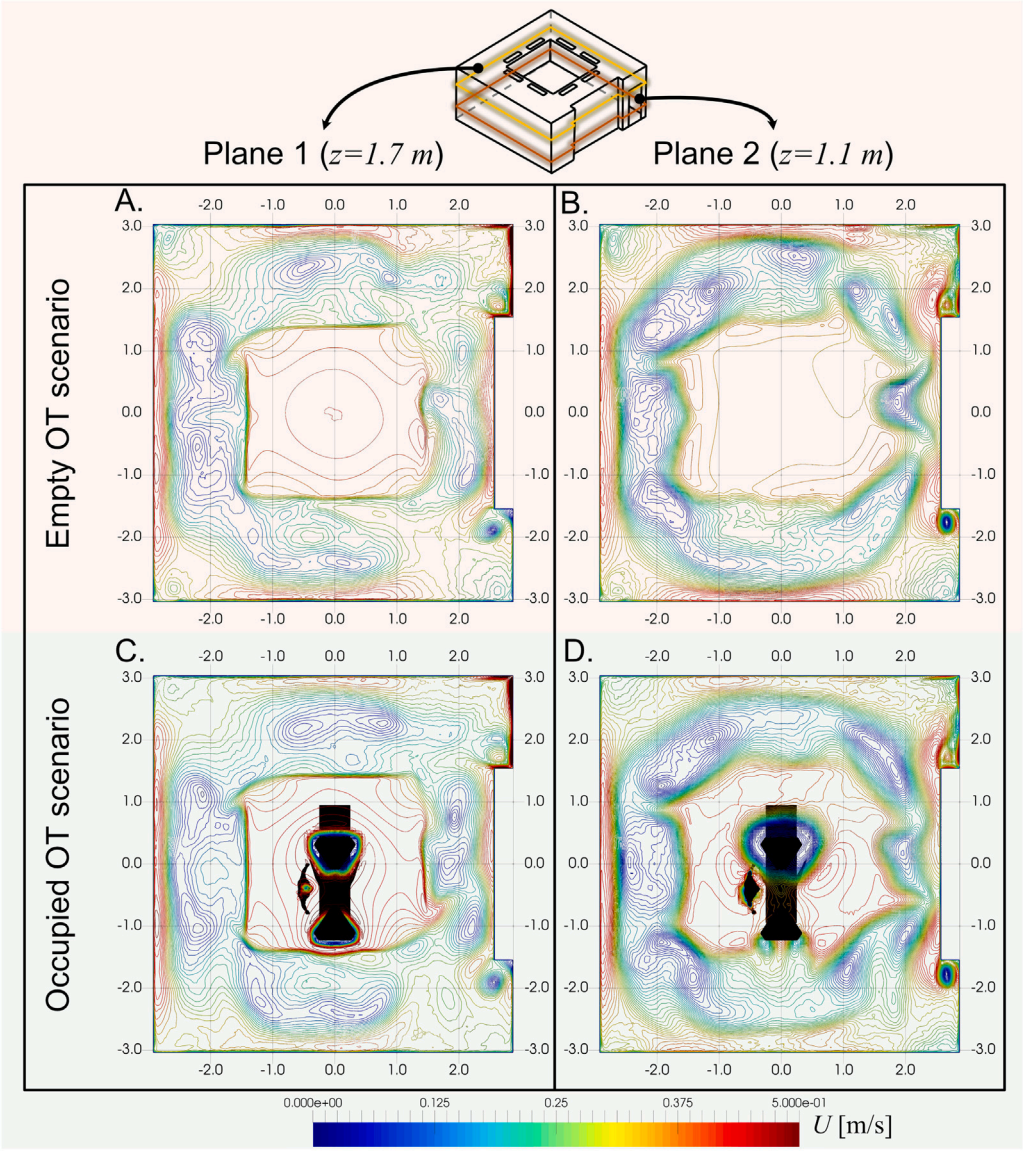

Fig. 7. Contours of velocity magnitude at selected planes for the empty and occupied scenarios. Velocity magnitude extracted with plane 1 at $z = 1.7$ m (left), and with Plane 2 at $z = 1.1$ m (right). (For interpretation of the references to colour in this figure legend, the reader is referred to the web version of this article.)

lower heights reveals the presence of high velocity gradients, particularly in areas that would typically be occupied by auxiliary personnel during medical procedures.

This distinct velocity pattern is indicative of turbulent flow, which can lead to increased mixing of airborne bioparticles. Consequently, there is a potential risk for the proliferation of nosocomial infections caused by these particles, as suggested by previous studies, such as the one by Kalantari and Patankar [75]. Even in the empty OT scenario, which represents an idealised condition, the formation of recirculation zones in regions less conducive to laminar flow presents an inherent risk of infection. This highlights the importance of understanding the complex flow dynamics within the operating theatre, not only for the optimisation of ventilation systems but also for the implementation of effective infection control measures.

For the occupied case, depicted in **C** and **D** of Fig. 7, the velocity contours in the outer region exhibit behaviour akin to the empty case, even near the scrub-room boundary. However, the intensity of the velocity gradient is noticeably enhanced. This observation underscores that a reduced occupation, primarily confined within the UCA zone, does not substantially alter the flow velocity pattern but does influence the levels of viscous shear stress.

In contrast, the flow patterns within the central UCA zone are significantly affected in the occupied scenario. As anticipated, the presence of obstacles, such as surgical lamps and personnel, introduces perturbations into the flow. These perturbations alter both the velocity distribution and its corresponding gradient. Specifically, in Plane 1, the lamps and the head of the standing occupant act as flow obstructions, accelerating the surrounding fluid and creating regions of high velocity and pronounced gradient, particularly around the lamps. These patterns are discernible in Plane 2 as well, albeit with reduced intensity, reflecting the natural deceleration of the flow at this lower elevation.

Velocity vector plots derived from time-averaged flow were extracted also at Plane 2 and at a vertical plane positioned in the middle of the UCA zone at $y = 0.0$ m, named as Plane 3, as illustrated in Fig. 8. These plots are colour-coded using the mean pressure field, normalised by density (p/ρ). The most striking feature in these plots is the formation of a global toroidal structure. In fact, upon reaching a quasi-steady state, the airflow exhibited an "inverted trumpet shape" pattern, consistent with the anticipation in Fig. 5(c). This pattern is characterised by a predominantly vertical downwash flow in the central region, induced by the UCA system, and a toroidal recirculation flow

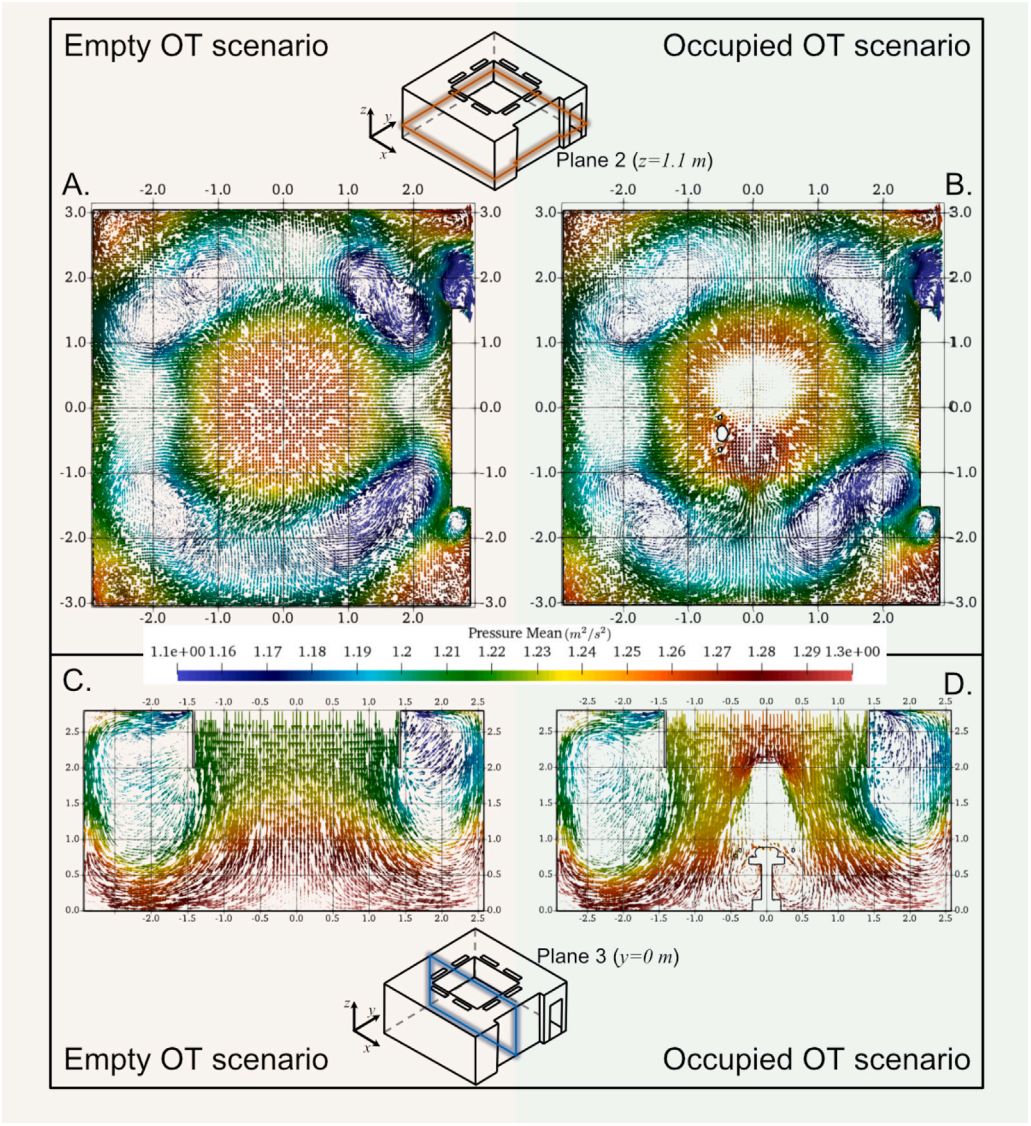

Fig. 8. Velocity vector plots, coloured by the density-normalised mean pressure field, visualised with Plane 2 at $z = 1.1$ m (top), and with Plane 3 at $y = 0,0$ m (bottom). (For interpretation of the references to colour in this figure legend, the reader is referred to the web version of this article.)

pattern near the theatre walls, but outside the UCA zone. As seen in **C** and **D** of Fig. 8, the toroidal flow pattern in the operating theatre exhibits a dynamic behaviour regardless of the scenario. The centre of the toroidal tube, while consistently positioned at approximately $z = 1$ m horizontally, varies vertically between $z = 1.6$ m and $z = 2.3$ m. This vertical undulation of the low-pressure centre, along with the absence of a discernible vortical centre in certain regions closer to the ceiling (as observed in the upper left location of Plane 3 in **C** of Fig. 8), suggests a flexible tubular structure rather than a strictly horizontal toroidal flow.

The velocity iso-contours in Fig. 7 and the velocity vector plots of the occupied case corroborate the influence of obstacles on the flow acceleration, particularly around the lamps. These are the first objects encountered by the inlet fluid, creating a low circulation zone between the lamps and the operating table, as clearly depicted in **B** and **D** of Fig. 8. Notably, the flow also exhibits significant disturbance under the operating table. Despite these obstacle-induced variations, the elevations of the toroidal centres in both the occupied and empty cases remain remarkably similar.

To further elucidate the toroidal flow pattern, coherent structures were constructed based on pressure iso-surfaces using the mean pressure field. The thresholds employed were $P = 101326.2$, 101326.32, 101326.39, and 101326.45 Pa, and the resulting structures are depicted in Fig. 9. These iso-surfaces confirm the presence of a quasi-toroidal structure around the UCA zone, which appears to meander vertically. Interestingly, two quasi-concentric toroids corresponding to the two higher threshold values are discernible, although not readily apparent in the plot. The pressure field within this toroidal structure decreases towards the centre of the enclosed region. Another remarkable feature is the formation of vertical tubular structures near the door leading to the scrub room and the opposite corner of the same wall, the most distant positions in the $x-$direction according to Fig. 5(c). These vertical structures are clearly linked to the high velocity zones identified previously, and therefore to recirculation zones in the vicinity of those corners.

5.2. Dissipation rate, Kolmogorov length, and TKE

The power spectra, while insightful, do not distinctly differentiate between laminar and turbulent flows in the analysed OT. Both flow behaviours were identified in the ultraclean area, which is anticipated to be laminar, and in the outer region. To delve deeper into the flow regime, we evaluated the rate of turbulent kinetic energy (TKE) dissipation, denoted as ϵ, throughout the domain. This facilitated the determination of the local Kolmogorov length scale, η_κ, via the relation

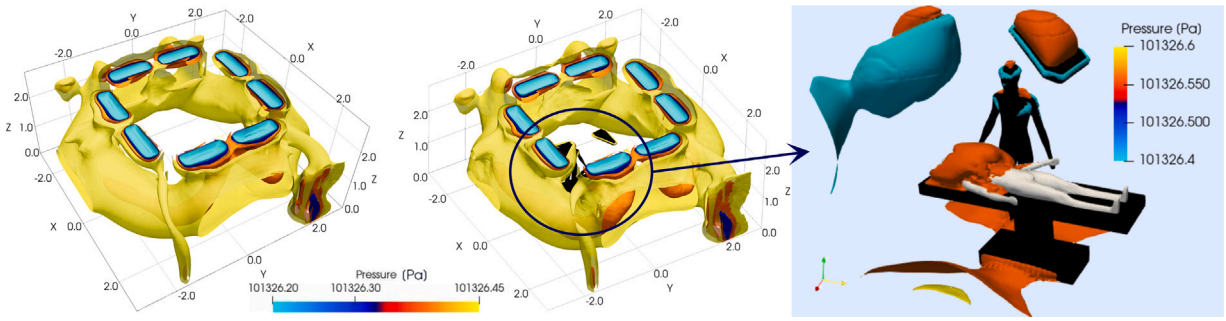

Fig. 9. Coherent structures based on pressure iso-surfaces. Left: empty OT case; Centre: partially occupied case; Right: Details around occupiers and obstacles. (For interpretation of the references to colour in this figure legend, the reader is referred to the web version of this article.)

$\eta_\kappa \approx (\nu^3/\epsilon)^{1/4}$, which is dependent solely on the kinematic viscosity and ϵ. To discern between laminar and turbulent flows, we used the following threshold for laminar flow dissipation:

$$\epsilon_l = \alpha\, \nu \left(\frac{U}{L}\right)^2 \tag{4}$$

Here, α is a scaling factor (set to one), and U, L, and ν represent the bulk flow velocity, a reference length, and flow viscosity, respectively. Using the mean inlet flow velocity and the OT's half-height as reference, the laminar regime threshold was estimated as $\epsilon_l = 1.2 \times 10^{-6}$ m^2/s^3. Spatial distributions of ϵ on Plane 3 are depicted in Fig. 10 **A** and **B** for the empty and occupied OT cases, respectively. We also examined ϵ distribution on a Plane 4, another midplane perpendicular to Plane 3 and aligned with the y-direction, as shown in **C** and **D**. Whereas for the empty case there is no major difference in the ϵ distribution, for the occupied scenario there is clearly an interesting pattern of alternating low and high ϵ within the UCA region, clearly induced by the presence of the lamps.

Considering the range of ϵ values and the ϵ_l threshold, we identified three flow regions. The low ϵ region ($\epsilon \leq 2.5 \times 10^{-7}$) is primarily confined to the UCA's upper part, near the ceiling inlet. The medium-range ϵ region, spanning between 2.5×10^{-7} and 5×10^{-6}, encompasses heights from 1.0 m to 2.0 m within the UCA. The rest of the OT exhibits high energy dissipation rates ($\epsilon \geq 5 \times 10^{-6}$). Using the threshold $\epsilon_l = 1.2 \times 10^{-6}$ m^2/s^3, we deduced that the flow is laminar in the first region, transitions in the medium-range, and becomes turbulent in the third. Notably, the spatial distributions of ϵ and that of η_κ in Fig. 10**G** mirror the inverted trumpet flow pattern seen in the airflow velocity field within similar theatres.

Upon contrasting the distribution of ϵ in the empty scenario with that in the partially occupied setting, it becomes evident that the low-ϵ region, which corresponds to a purely laminar flow, is further restricted to the upper part of the operating theatre. The introduction of lamps around $z = 2.0$ m confines this low-dissipation region to the theatre's ceiling and canopy's walls, even inducing a high-dissipation zone directly above them. Fortunately, in such environments, the air delivered by the UCA system is, in principle, largely devoid of particles and potential contaminants. Therefore, while turbulent mixing at this height might not critically affect the room's sanitary conditions, a pronounced mixing current is evident by the time the UCA flow reaches the surgeons and instrument tables. This design seems to accentuate the transition to turbulence, challenging any preliminary assumptions of laminar flow in such spaces.

The dissipation rate ϵ is plotted along horizontal lines on the XZ-midplane at various heights of the empty OT in **E** of Fig. 10. Trends and bounds were consistent on the YZ-midplane. The flow exhibits a lower energy dissipation rate than the laminar threshold within the UCA, especially near the ceiling. However, this laminar behaviour transitions to turbulence as the flow descends. By $z = 0.6$ m, the dissipation rate surpasses the threshold ϵ_l. The turbulent kinetic energy (TKE) was also analysed, with profiles shown in **F** of Fig. 10. The TKE remains minimal within the UCA, especially near the ceiling, but escalates towards the floor. Outside the UCA, TKE levels are comparable to those near the floor within the UCA, but they markedly increase, reaching up to four orders of magnitude at the ceiling in the peripheral region. Notably, at $z = 1.0$ m, a homogenisation effect seems to induce equivalent TKE levels throughout the operating theatre. Although not depicted in Fig. 10, in the occupied OT scenario, the situation appears more complex as both the dissipation rate and TKE attain elevated values even within the UCA, specifically just above the operating table. This heightened TKE could foster the emergence of robust recirculation zones near any obstacle within the UCA, which should be considered when selecting a specific layout for any procedure.

While the UCA effectively maintains a laminar-like flow at the theatre's core, turbulence manifests around $z = 1.0$ m and is prevalent throughout a significant portion of the OT. The corners adjacent to the floor display heightened turbulence and vorticity, which persists as the flow ascends along the walls. Essentially, the UCA zone effectively sustains a laminar flow at the theatre's centre, but turbulence emerges around the critical height of the operating table and dominates most of the theatre thereafter. This turbulent behaviour is especially pronounced at the theatre's corners, continuing as the flow moves towards the exhaust vents.

These set of results also allowed us to check again the mesh quality's adequacy for our computational model, as validated by results in Fig. 10, especially in **G** and **H**. The mesh density adhered to the resolution criteria for qDNS simulations, as mandated by our model. The cell-based length to local Kolmogorov ratio consistently remained below $L/\eta_\kappa \approx 10$ near the theatre and canopy walls, and only exceeded the threshold of $L/\eta_\kappa = 14$ in the outer region close to the ceiling.

To further enrich our analysis, we investigated the convection of kinetic energy (KE) and turbulent kinetic energy (TKE) at two specific vertical lines within the operating theatre. These lines are designated as Z_0 and Z_1, representing locations inside and outside the clean zone, respectively. Instantaneous and time-averaged velocity data were collected at 0.1-second intervals over a simulation duration of 18 s. Each line extends over a length of 2.5 m, ranging from heights of 0.15 m to 2.65 m, and comprises 2048 data points.

Utilising this dataset, we calculated the normalised KE and TKE values. Space–time diagrams were then constructed to scrutinise the convection behaviour of these energy terms along the vertical lines, as illustrated in Fig. 11. Both the KE and TKE maps were normalised using a characteristic kinetic energy term, U_O^2, based on the average air injection velocity at $z = 2$ m ($U_0 = 0.38$ m/s). To facilitate the identification of the advection speeds of KE and TKE structures, three sloping lines were superimposed on the space–time maps. These lines represent the normalised advection velocities of the KE and TKE structures, also scaled by the average air injection velocity U_0 in the operating theatre.

In terms of variable intensity, notable differences between the empty and occupied operating theatres (OTs) are evident. Specifically, kinetic energy (KE) disparities are most pronounced at mid-height,

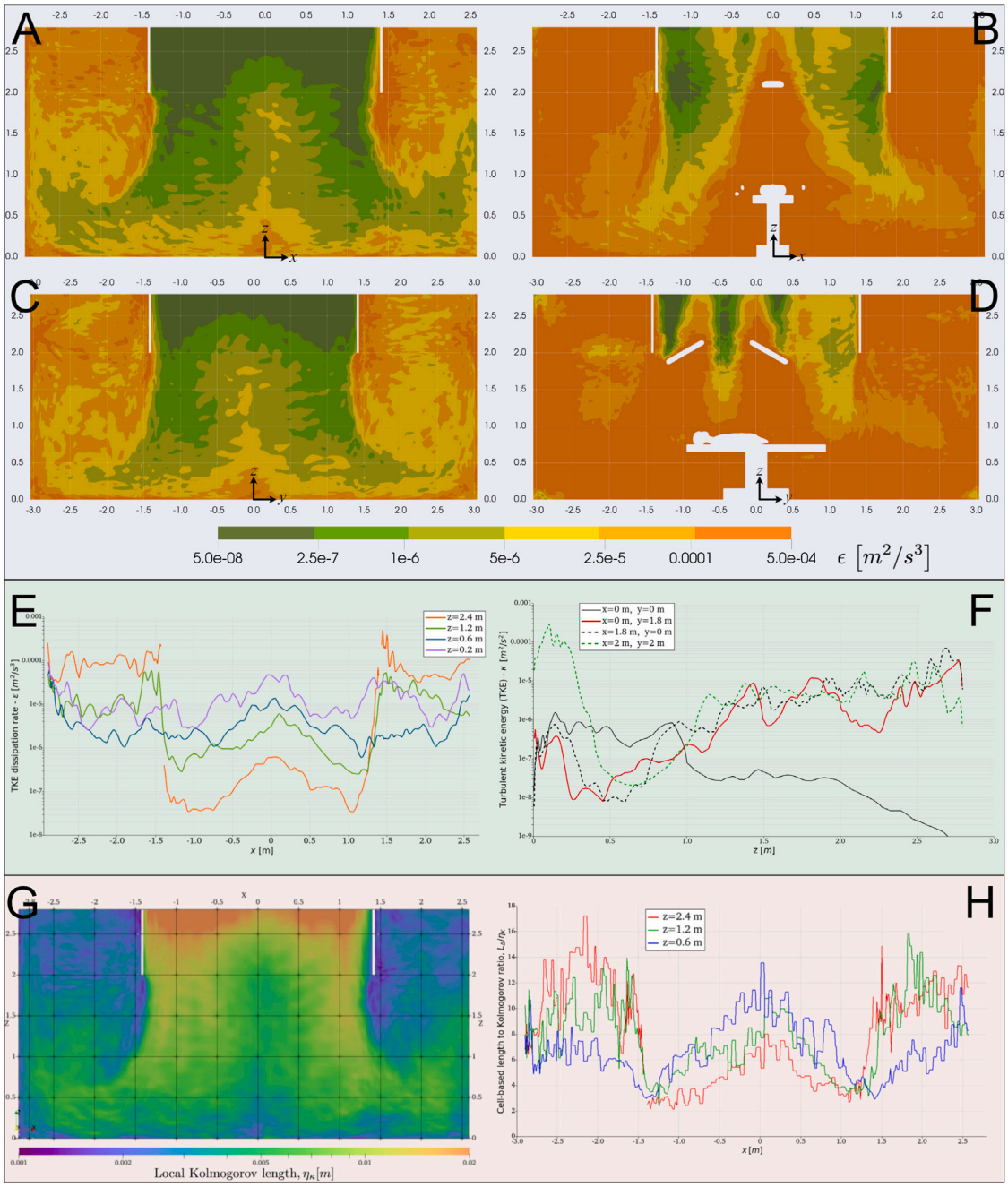

Fig. 10. Contours of dissipation rate and local Kolmogorov scale in theatre's midplanes (**A**,**B**,**C**,**D**,**G**), and profiles of dissipation rate, TKE, and cell-based length to Kolmogorov ratio L_Δ/η_κ (**E**,**F**,**H**). (For interpretation of the references to colour in this figure legend, the reader is referred to the web version of this article.)

whilst turbulent kinetic energy (TKE) variations are more noticeable near the floor along the inner line Z_0, as depicted in Fig. 11**A**,**B** and Fig. 11**E**,**F**, respectively. In both instances, the occupied OT exhibits elevated levels of KE and TKE along the Z_0 line. This amplification is attributable to the presence of obstacles, which constrict the flow area, thereby increasing fluid velocity and consequently inducing flow instabilities that elevate both KE and TKE.

It is imperative to acknowledge that although the primary flow direction is downward along Z_0 and upward along Z_1, the flow is intrinsically three-dimensional. This complexity introduces transverse components that significantly influence the advection velocities of KE and TKE structures. Upon examining Fig. 11**C**,**D** and Fig. 11**G**,**H**, it becomes apparent that the advection speeds of these structures along the Z_0 line are relatively consistent between scenarios. However, a subtle divergence is observed along the outer line Z_1. Specifically, in the empty OT, the advection speed approximates $5U_0$, whilst in the occupied OT, it is closer to $9U_0$. Interestingly, the intensities of KE and TKE along Z_1 are relatively similar between the two scenarios, despite the marked difference in advection speeds.

In the analysis of the KE and TKE space–time diagrams, it becomes evident that the inclusion of obstacles within the clean zone not only intensifies turbulent effects in their vicinity but also globally augments the advection of airflow and, consequently, of contaminants. While localised stagnation zones for contaminant accumulation are present, the behaviour of the external vortex is modified, corroborating observations made in Fig. 8. This leads to an increased entrainment rate of the variables, thereby accelerating the cleansing process within this section of the operating theatre. This observation of enhanced advective behaviour in the occupied theatre is further confirmed with a detailed analysis on ventilation efficiency presented in next section.

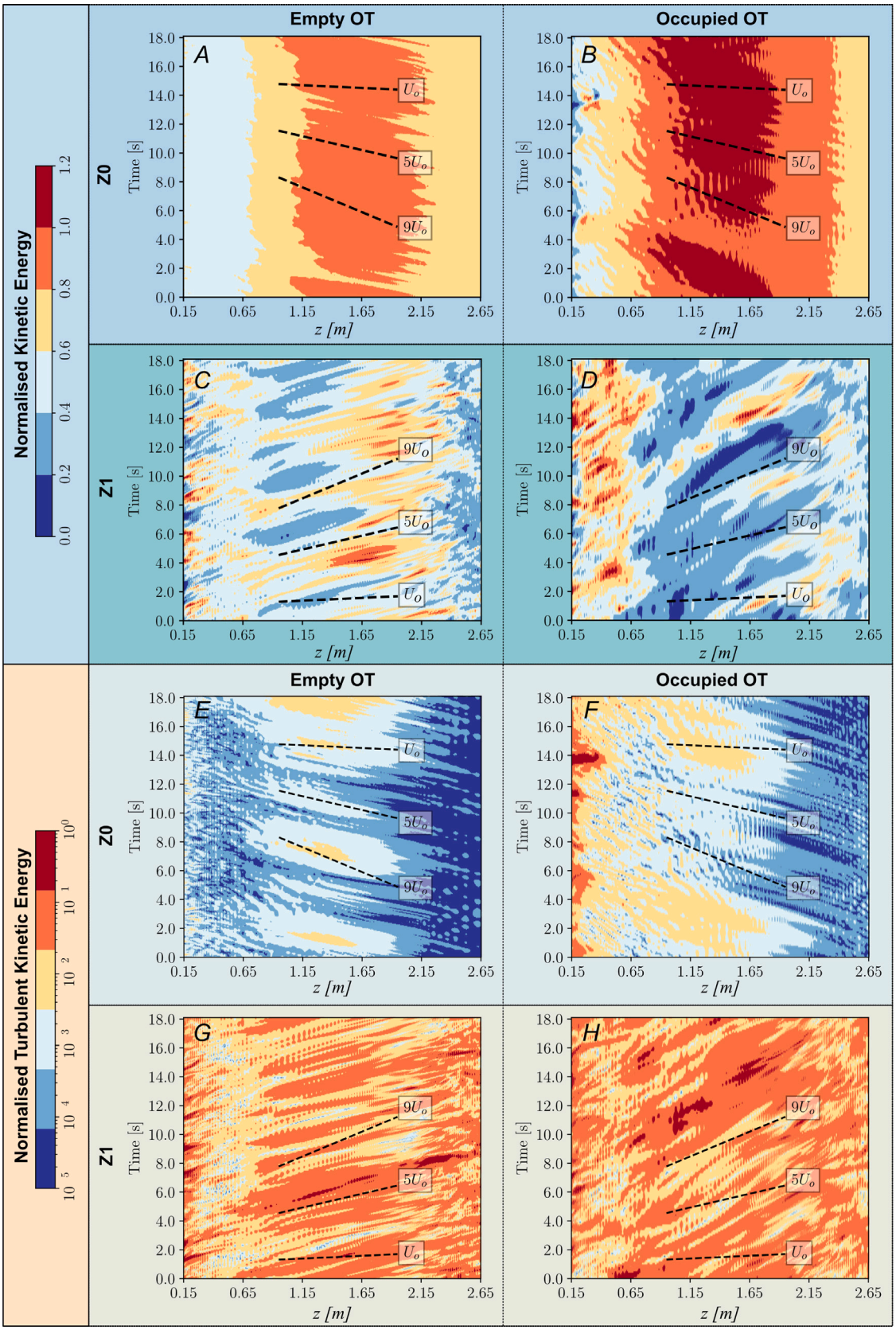

Fig. 11. Space–time diagrams showing convection of kinetic energy (**A**,**B**,**C**,**D**) and turbulent kinetic energy (**E**,**F**,**G**,**H**), along two vertical lines Z_0 and Z_1. Both maps are normalised with U_0^2. The dashed lines indicated the slopes in terms of the average inlet velocity. (For interpretation of the references to colour in this figure legend, the reader is referred to the web version of this article.)

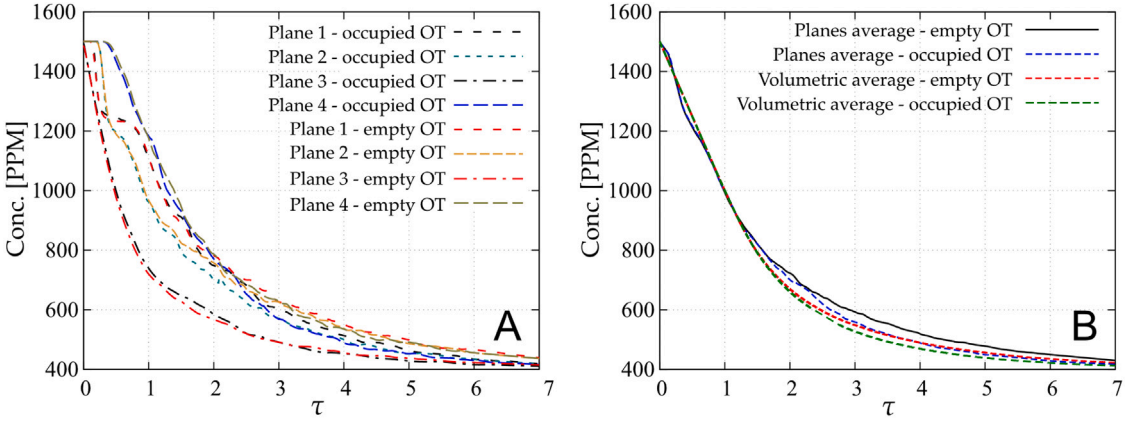

Fig. 12. **A.** Comparison of concentration decay at different planes; **B.** Plane and volumetric average concentration decay. Results shown for both empty and occupied operating theatre. (For interpretation of the references to colour in this figure legend, the reader is referred to the web version of this article.)

Table 1
Characteristic time measured in each case to be used as normalisation factor for non-dimensional time τ.

Scenario	$t_{CO_2=1000\,[PPM]}$, (s)
Empty OT	14.707
Occupied OT	14.673

5.3. Ventilation efficiency

As delineated in the methodology section, the tracer gas decay method initiated with a baseline concentration of 1500 [PPM], targeting a mean concentration of 400 [PPM]. The decay analysis was undertaken through two distinct strategies: the first leveraging an average volumetric value across the entire computational domain, derived from the integral of the CO_2 concentration throughout the room divided by its volume, for both the empty and occupied scenarios. The second strategy employed a per-plane average area value derived from four planes (two horizontal and two vertical), as depicted in Figs. 7 and 8, and detailed within the methodology.

To streamline the results analysis, a characteristic time, denoted as $t_{CO_2=1000\ [PPM]}$, was introduced to normalise the temporal evolution of the CO_2 concentration. This metric represents the duration needed for the concentration to reduce from 1500 [PPM] to a benchmark concentration of 1000 [PPM], the latter being the advised upper limit for enclosed environments. Consequently, a non-dimensional time $\tau = t/t_{CO_2=1000\ [PPM]}$ was defined, with the characteristic times for both scenarios documented in Table 1.

The simulations spanned approximately 175 s, ensuring a quasi-steady state for the CO_2 concentration over seven characteristic times ($\tau = 7$) in both scenarios. Fig. 12**A** illustrates the concentration decay across various monitored planes in both conditions. Notably, an exponential decay pattern is evident across all planes, converging towards a 400 [PPM] threshold. The p3 plane, intersecting the canopy, exhibited the swiftest decay due to direct exposure to UCA inflow, while the p4 plane, situated outside the canopy, demonstrated the slowest decay rate. Despite these initial disparities, the decay curves converge to comparable levels as τ approaches 5, indicating a uniform rate of concentration reduction across all planes, irrespective of the OT's occupancy status.

To evaluate the influence of room occupancy on the ventilation efficiency of the OT, an average CO_2 concentration decay value was derived from the per-plane decay curves of all planes. This was complemented by computing a volumetric decay, which involved integrating the concentration across the entire volume of the OT, thereby offering a comprehensive view of the concentration dynamics throughout the whole environment. A detailed comparison between the planes-average decay and the volumetric decay, under both empty and occupied conditions, is presented in Fig. 12**B**. This figure shows the juxtaposition of the decay profiles obtained by both approaches, facilitating an understanding of the nuanced evolution of the ventilation dynamics in both scenarios.

Contrary to what one might anticipate, the concentration decay is more pronounced in the occupied OT scenario. This phenomenon is hypothesised to be a consequence of the augmented kinetic energy (KE) and turbulent kinetic energy (TKE) values, brought about by the presence of objects within the room. These objects foster the formation of intricate flow patterns and vortical structures, as previously illustrated, thereby enhancing the airflow and facilitating the transport of contaminants. Consequently, the CO_2 advection rates are heightened, resulting in a more efficient room ventilation compared to the empty OT scenario.

A deeper appreciation of this finding can be reached by examining the behaviour of concentration in specific planes and at different characteristic times. Fig. 13 delineates the concentration dynamics in plane 1 for $\tau = 1$, 3, and 7 in both scenarios. Initially, the CO_2 distributions are somewhat analogous in both cases, albeit the occupied scenario exhibits regions of heightened CO_2 concentration due to the presence of objects. As the simulation advances, a more substantial reduction in the contaminant concentration is evident in the occupied scenario, culminating in near-total depletion at the final time marker.

Similarly, an analysis of plane 3, depicted in Fig. 13, reveals that the occupied scenario seems characterised by an initial accumulation of CO_2 near the objects. However, the strategic placement of these objects alters the CO_2 dynamics compared to the empty scenario, which exhibits a higher concentration in the lower corner. The vortical structures induced by the objects thus steer the CO_2 towards the outlets, expediting the pollutant evacuation process.

To discern the disparity between the scenarios under consideration, ventilation efficiency serves as a pivotal metric. Defined as the efficacy of pollutant removal from a room, it is a crucial parameter in ventilation studies [76]. A prevalent formulation, devised by [26], is given by:

$$\gamma = \frac{C_e - C_s}{C - C_s} \times 100\% \tag{5}$$

Here, γ denotes the ventilation efficiency, C_e is the pollutant concentration at the exhaust, C_s represents the concentration at the supply, and C is the room's average concentration. In this study, C_s is consistently 400 [PPM], while C could be the volumetric or planes average value delineated in Fig. 12. The concentration at various exhaust points (Door, Outlet, and Window) was meticulously recorded at each time instance.

As depicted in Figs. 14(a) to 14(c), the CO_2 concentration at the outlets commences its decline after approximately one characteristic

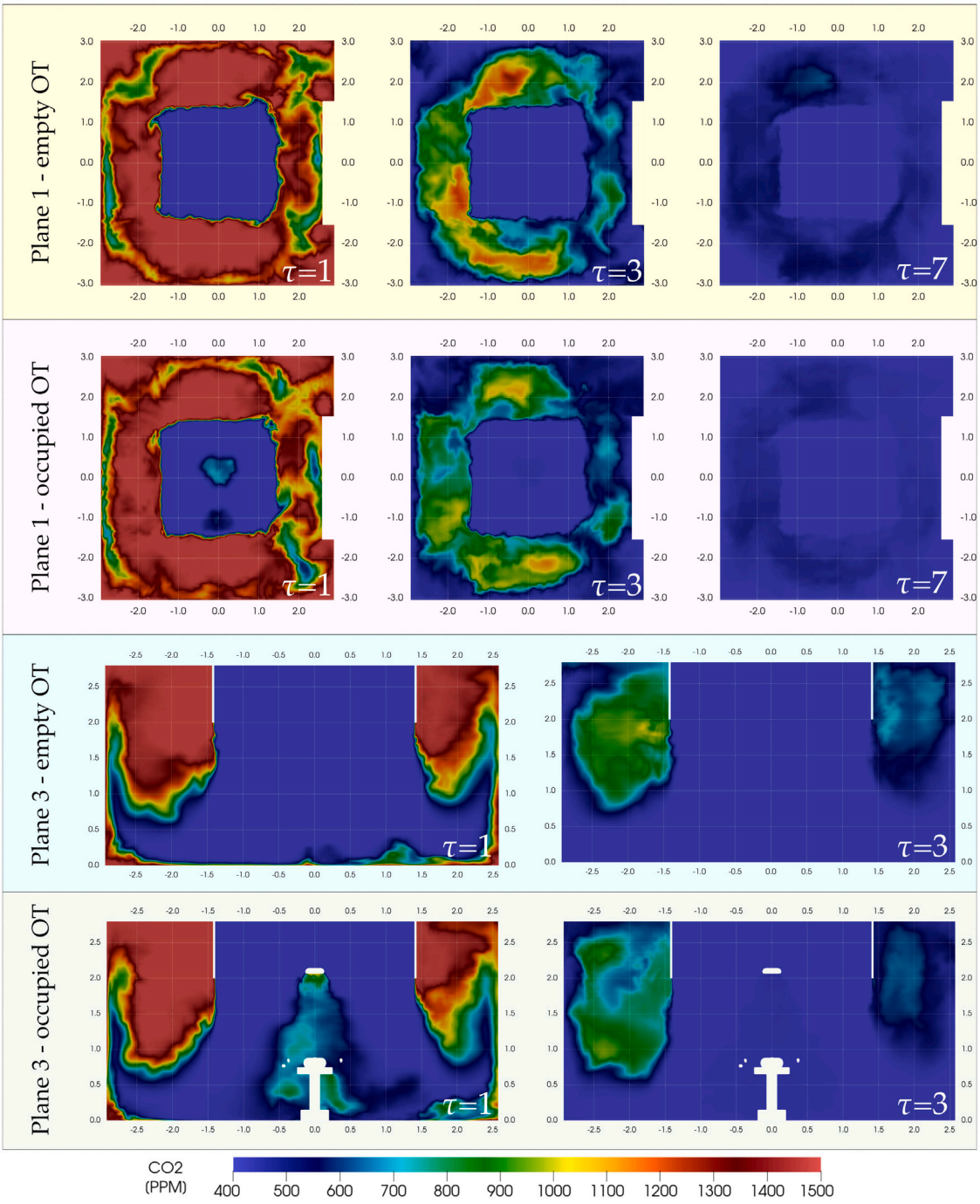

Fig. 13. Temporal evolution of CO_2 concentration in both scenarios, empty and occupied OT. Snapshots at $\tau = 1, 3$, and 7 for Plane 1, and at $\tau = 1, 3$ for Plane 3. (For interpretation of the references to colour in this figure legend, the reader is referred to the web version of this article.)

time, stabilising at the stipulated threshold over seven characteristic times. Notably, the ceiling outlets exhibit a protracted duration to attain the minimum value compared to other exhausts.

Utilising the data acquired from each outlet, we computed the corresponding ventilation efficiencies, illustrated in the lower row of Fig. 14. A noteworthy observation is the initial surge above 100%, followed by a gradual reduction, a phenomenon attributed to the delayed onset of concentration decline at the exhaust relative to the volumetric value, as expressed in Eq. (5). The occupied scenario demonstrates superior CO_2 extraction efficiency across all exhausts, corroborating the findings from the volumetric decay analysis.

For a comprehensive understanding, we averaged the concentration decay across all outlets and recalculated the efficiency, the details of which are presented in Fig. 15**A**. The occupied case maintains an efficiency bracket of 80% to 100%, outperforming the empty case which fluctuates between 60% and 80%.

The CO_2 concentration dynamics are intrinsically tied to the flow patterns, a relationship vividly portrayed in Fig. 15**B**. This figure, representing the occupied operating theatre at the normalised time $\tau = 1$, unveils the juxtaposition of velocity isocontours in plane 1 and the orthogonal planes depicting CO_2 contours. It elucidates that regions of diminished velocity harbour elevated concentration levels, nearing 1200 [PPM] in this instance. Conversely, walls neighbouring areas, characterised by heightened velocity, exhibit a concentration nearing the minimal threshold of 400 [PPM]. A critical insight gleaned from the

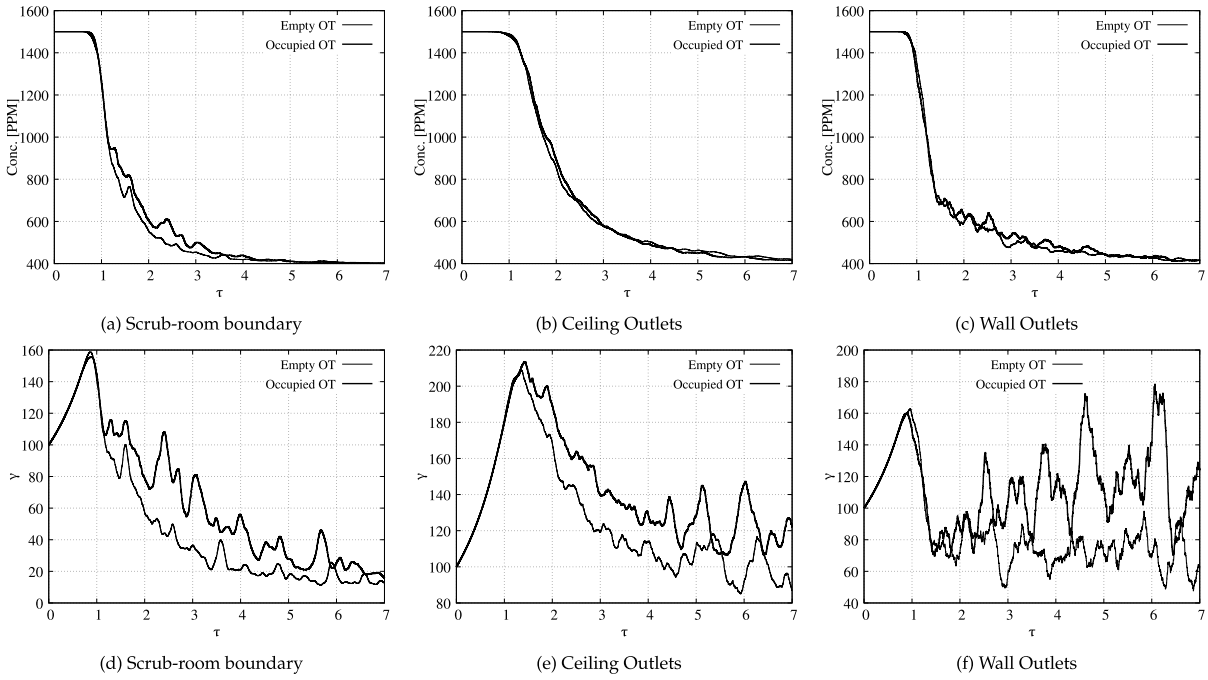

Fig. 14. Exhausts concentration decay (top row), and ventilation efficiency of every exhaust (bottom row), for both empty and occupied scenarios.

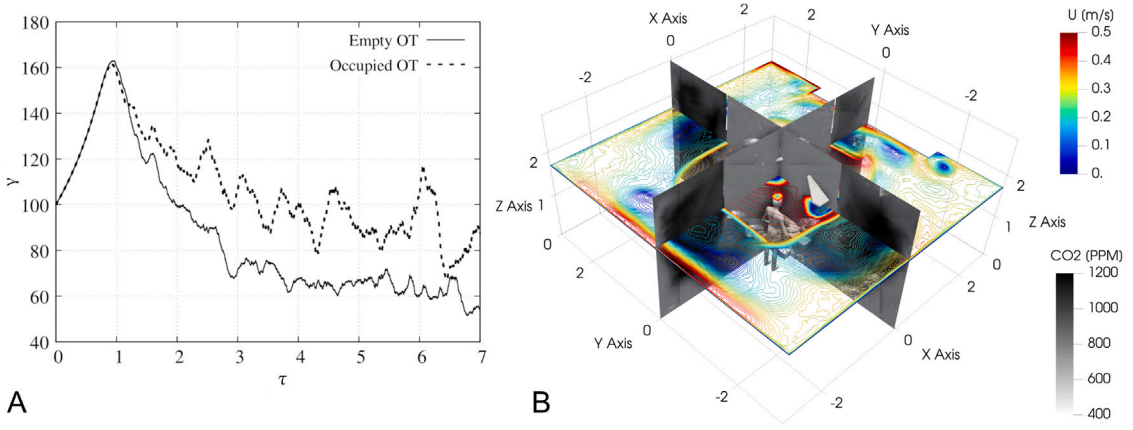

Fig. 15. **A** Global ventilation efficiency for empty (Emp.) and occupied (Occ.) OT; **B** Correlation between velocity magnitude contours and CO_2 concentration at $\tau = 1$. (For interpretation of the references to colour in this figure legend, the reader is referred to the web version of this article.)

velocity vectors in Fig. 8 is the correlation between the vortex centres of the primary toroidal structures, associated with low-pressure zones, and the peak CO_2 concentration zones.

6. Conclusions

In this study, we have undertaken a comprehensive analysis of airflow patterns within a surgical operating theatre, leveraging a quasi-DNS CFD model corroborated with ultrasound-based anemometry data. This innovative approach, which integrates computational and experimental methodologies, has facilitated a nuanced understanding of the turbulent behaviours and flow patterns in different regions of the theatre, thereby offering insights into potential areas of microbial air contamination and ventilation inefficiencies.

The CFD model, grounded in the precise dimensions and specifications of the HVAC system of a specialist orthopaedic hospital's operating theatre, was validated through meticulous anemometer surveys. This validation process underscored the efficacy of our methodology in capturing the intricacies of airflow patterns more accurately than traditional approaches.

Our analysis extended to evaluating the impact of partial occupancy, incorporating elements such as lamps, medical personnel, and a patient on the operating table, on both the airflow patterns and ventilation performance. This was complemented by a ventilation efficiency study employing the tracer gas method, revealing that the occupied scenario surprisingly fostered more efficient CO_2 extraction, a finding corroborated by volumetric decay analysis.

Despite the Ultra Clean Air (UCA) zone's design intending to maintain a laminar flow, our results indicate a transition to turbulent flow occurring at approximately $z = 1.0$ m above ground level. This turbulence, characterised through various measures including turbulent kinetic energy profiles and velocity time history, persists and even escalates in the theatre corners, challenging the conventional expectations of the UCA design. The flow dynamics, resembling an "inverted trumpet" airflow pattern, foster a quasi-toroidal flow that circulates around the central region, a phenomenon that is largely maintained in the occupied scenario.

The occupied scenario introduced notable variations, particularly the acceleration of flow near the lamps and the emergence of vortical

structures due to fluid-obstacle interactions. Despite these alterations, certain characteristics, such as the toroidal behaviour and its spatial positioning, remained relatively consistent with the empty scenario.

The study also unveiled the presence of low-velocity regions or "bulges" predominantly in the outer region surrounding the central UCA zone, with a pronounced manifestation at lower elevations. These regions, characterised by high velocity gradients, are typically occupied by auxiliary personnel, highlighting potential areas of concern during surgical procedures.

The fidelity of our study illustrates that while the inclusion of objects such as lamps, a standing person, an operating table and a lying person might appear to minimally affect the overall large-scale airflow – preserving recirculation zones and coherent pressure structures – the scenario changes when we focus on small-scale phenomena. Specifically, the results of the TKE profiles, dissipation rates and advection of KE and TKE structures delve into the nuances of transitions from flow to turbulence and zones of localised turbulence, revealing significant alterations between the two scenarios that merit consideration in specific arrangements. These two perspectives indicate that, depending on the scale of the phenomenon under study, it is possible to simultaneously find features that change minimally and, at the same time, others that are profoundly affected by the presence of different types of obstacles and occupancy levels.

Similarly, our study challenges the prevailing notion of laminar airflow in operating theatres, demonstrating that even minimal obstructions can precipitate noticeable changes, especially in terms of localised turbulence. These findings highlight the potential implications for asepsis levels within the operating theatre. In contrast, when the analysis focuses on large-scale phenomena or relies on aggregate volumetric measurements, the impact of layout selection appears to have little impact. This nuanced understanding underlines the complexity of airflow dynamics in occupied spaces and the importance of the scale of the phenomena studied when assessing the effects of layout and obstructions on airflow characteristics in operating theatres.

Our findings suggest that the current UCA theatre design, while effective in removing bacteria-carrying particles through strong downflow in the clean zone, harbours inherent risks. The turbulent regime induced by obstructions, even under reduced occupancy, engenders recirculation zones, potentially escalating the risk of surgical site infections (SSIs).

In light of these insights, it becomes imperative to revisit the design of UCA operating theatres to foster more controlled flow conditions, thereby mitigating the risks associated with fast down-flows. Leveraging detailed computational modelling alongside a robust experimental setup could pave the way for design modifications that enhance the microbiological performance of these theatres.

Looking forward, there is a pressing need to delve deeper into understanding the thermal effects arising from various elements within the theatre, including warming blankets and the surgical team, to foster HVAC systems that are both efficient and safe. This study lays a robust foundation for such future endeavours, steering towards operating theatres that are not just technically advanced but also secure in mitigating infection risks [74].

7. Acknowledgements

We acknowledge the support of the University of Birmingham and the use of the BlueBEAR high-performance computing facility. We acknowledge the support of the Royal Orthopaedic Hospital NHS Foundation Trust. The computations described in this paper were performed using the University of Birmingham's BlueBEAR HPC service. See http://www.birmingham.ac.uk/bear for more details.

CRediT authorship contribution statement

Carlos A. Duque-Daza: Writing – review & editing, Writing – original draft, Supervision, Software, Methodology, Investigation, Funding acquisition, Formal analysis, Conceptualization. **Jairo Murillo-Rincón:** Writing – review & editing, Visualization, Validation, Software, Investigation. **Andrés S. Espinosa-Moreno:** Visualization, Validation, Software, Data curation. **Federico Alberini:** Writing – review & editing, Methodology, Formal analysis, Conceptualization. **Alessio Alexiadis:** Methodology, Formal analysis, Conceptualization. **Diego A. Garzón-Alvarado:** Methodology, Formal analysis, Conceptualization. **Andrew M. Thomas:** Writing – review & editing, Writing – original draft, Methodology, Formal analysis, Conceptualization. **Mark J.H. Simmons:** Supervision, Methodology, Formal analysis, Conceptualization.

Declaration of competing interest

The authors declare that they have no known competing financial interests or personal relationships that could have appeared to influence the work reported in this paper.

Data availability

Data will be made available on request.

References

[1] P. Marre, R. Villet, Anatomy theaters in the history and teaching of surgery, J. Visc. Surg. 157 (3) (2020) S73–S76.
[2] B.J. Clemons, The first modern operating room in America, AORN J. 71 (1) (2000) 164–170.
[3] A. Spagnolo, G. Ottria, D. Amicizia, F. Perdelli, M. Cristina, Operating theatre quality and prevention of surgical site infections, J. Prev. Med. Hyg. 54 (3) (2013) 131–137.
[4] Y.W. Najjar, Z.M. Al-Wahsh, M. Hamdan, M.Y. Saleh, Risk factors of orthopedic surgical site infection in Jordan: A prospective cohort study, Int. J. Surg. Open 15 (2018) 1–6.
[5] J. Charnley, Postoperative infection after total hip replacement with special reference to air contamination in the operating room, Clin. Orthop. Relat. Res. 87 (1972) 167–187, http://dx.doi.org/10.3109/9780203214237-125.
[6] W. Waugh, John Charnley: The Man and the Hip, Springer Science & Business Media, 2012.
[7] O. Lidwell, E. Lowbury, W. Whyte, R. Blowers, S. Stanley, D. Lowe, Airborne contamination of wounds in joint replacement operations: the relationship to sepsis rates, J. Hosp. Infect. 4 (2) (1983) 111–131, http://dx.doi.org/10.1016/0195-6701(83)90041-5, URL https://www.sciencedirect.com/science/article/pii/0195670183900415.
[8] L.A. Reynoldsm, E.M. Tansey, Early Development of Total Hip Replacement, WT CTR for the History of Medicine at UCL, 2007, URL https://www.ebook.de/de/product/6534451/early_development_of_total_hip_replacement.html.
[9] W. Whitfield, Brief history of laminar flow clean room systems, 1981.
[10] W. Whitfield, J. Mashburn, W. Neitzel, A new principle for airborne contamination control in clean rooms and work stations, in: Symposium on Cleaning and Materials Processing for Electronics and Space Apparatus, ASTM International, 1963, pp. 979–988.
[11] D. Holbrook, Controlling contamination: the origins of clean room technology, History Technol. 25 (3) (2009) 173–191.
[12] J. McDade, J. Whitcomb, E. Rypka, W. Whitfield, C. Franklin, Microbiological studies conducted in a vertical laminar airflow surgery, JAMA 203 (2) (1968) 125–130, http://dx.doi.org/10.1001/jama.1968.03140020053013, arXiv:https://jamanetwork.com/journals/jama/articlepdf/337300/jama_203_2_013.pdf.
[13] N. guideline NG157, Joint replacement (primary): hip, knee and shoulder, Methods (2020).
[14] W. Popp, C. Alefelder, S. Bauer, G. Daeschlein, P. Geistberger, S. Gleich, C. Herr, N.-O. Hübner, L. Jatzwauk, W. Kohnen, R. Külpmann, F. Lemm, B. Loczenski, J. Spors, P. Walger, M. Wehrl, K.-D. Zastrow, M. Exner, Air quality in the operating room: Surgical site infections, HVAC systems and discipline – position paper of the german society of hospital hygiene (DGKH), GMS Hyg. Infect. Control; 14:Doc20 (2019) http://dx.doi.org/10.3205/DGKH000335.
[15] H. Dale, A.M. Fenstad, G. Hallan, L.I. Havelin, O. Furnes, S. Overgaard, A.B. Pedersen, J. Kärrholm, G. Garellick, P. Pulkkinen, A. Eskelinen, K. Mäkelä, L.B. Engesæter, Increasing risk of prosthetic joint infection after total hip arthroplasty, Acta Orthop. 83 (5) (2012) 449–458, http://dx.doi.org/10.3109/17453674.2012.733918.

[16] J.P. Nelson, A.R. Glassburn, R.D. Talbott, J.P. McElhinney, The effect of previous surgery, operating room environment, and preventive antibiotics on postoperative infection following total hip arthroplasty., Clin. Orthop. Relat. Res. (1980) 167–169.

[17] R.P. Evans, Current concepts for clean air and total joint arthroplasty: Laminar airflow and ultraviolet radiation: A systematic review, Clin. Orthop. Relat. Res. 469 (4) (2011) 945–953, http://dx.doi.org/10.1007/s11999-010-1688-7.

[18] A. Thomas, M. Simmons, The effectiveness of ultra-clean air operating theatres in the prevention of deep infection in joint arthroplasty surgery, Bone Joint J. 100-B (10) (2018) 1264–1269, http://dx.doi.org/10.1302/0301-620x.100b10.bjj-2018-0400.r1.

[19] A. Agodi, F. Auxilia, M. Barchitta, M. Cristina, D. D'Alessandro, I. Mura, M. Nobile, C. Pasquarella, S. Avondo, P. Bellocchi, R. Canino, C. Capozzi, R. Casarin, M. Cavasin, P. Contegiacomo, M.G. Deriu, F.R. Evola, P. Farsetti, A. Grandi, D. Guareschi, A.M. Longhitano, G. Longo, R. Malatesta, P. Marenghi, F. Marras, A. Maso, A.R. Mattaliano, M.T. Montella, U. Moscato, P. Navone, M.A. Romeo, F. Rossi, M. Ruffino, C. Santangelo, M. Sartini, G. Sessa, S. Tardivo, P.T. Leali, M.V. Torregrossa, P. Vitali, Operating theatre ventilation systems and microbial air contamination in total joint replacement surgery: results of the GISIO-ISChIA study, J. Hosp. Infect. 90 (3) (2015) 213–219, http://dx.doi.org/10.1016/j.jhin.2015.02.014.

[20] P.D. McGovern, M. Albrecht, K. G. Belani, C. Nachtsheim, P.F. Partington, I. Carluke, M.R. Reed, Forced-air warming and ultra-clean ventilation do not mix, J. Bone Joint Surg. Brit. Vol. 93-B (11) (2011) 1537–1544, http://dx.doi.org/10.1302/0301-620X.93B11.27124, arXiv:https://doi.org/10.1302/0301-620X.93B11.27124.

[21] S.M. McHugh, A.D.K. Hill, H. Humphreys, Laminar airflow and the prevention of surgical site infection. More harm than good? Surgeon 13 (1) (2015) 52–58, http://dx.doi.org/10.1016/j.surge.2014.10.003.

[22] P. Bischoff, N. Kubilay, B. Allegranzi, M. Egger, P. Gastmeier, Effect of laminar airflow ventilation on surgical site infections: a systematic review and meta-analysis, Lancet Infect. Dis. 17 (5) (2017) 553–561.

[23] N. Massarotti, A. Mauro, D. Sainas, S. Marinetti, A. Rossetti, A novel procedure for validation of flow simulations in operating theaters, Sci. Technol. Built Environ. 25 (5) (2019) 629–642.

[24] S. Saran, M. Gurjar, A. Baronia, V. Sivapurapu, P.S. Ghosh, G.M. Raju, I. Maurya, Heating, ventilation and air conditioning (HVAC) in intensive care unit, Crit. Care 24 (1) (2020) http://dx.doi.org/10.1186/s13054-020-02907-5.

[25] P. Gastmeier, A.-C. Breier, C. Brandt, Influence of laminar airflow on prosthetic joint infections: a systematic review, J. Hosp. Infect. 81 (2) (2012) 73–78, http://dx.doi.org/10.1016/j.jhin.2012.04.008.

[26] M. Sandberg, What is ventilation efficiency? Build. Environ. 16 (2) (1981) 123–135.

[27] T. van Hooff, B. Blocken, CFD evaluation of natural ventilation of indoor environments by the concentration decay method: CO2 gas dispersion from a semi-enclosed stadium, Build. Environ. 61 (2013) 1–17, http://dx.doi.org/10.1016/j.buildenv.2012.11.021, https://www.sciencedirect.com/science/article/pii/S0360132312003216.

[28] F. Wang, I. Permana, D. Rakshit, B.Y. Prasetyo, Investigation of airflow distribution and contamination control with different schemes in an operating room, Atmosphere 12 (12) (2021) 1639.

[29] J. Chao, X. Mu, Y. Xue, F. Li, W. Li, C.-H. Lin, J. Pei, Q. Chen, A modified tracer-gas decay model for ventilation rate measurements in long and narrow spaces, Indoor Built Environ. 23 (7) (2014) 1012–1020.

[30] S. Sadrizadeh, A. Afshari, T. Karimipanah, U. Hakansson, P. Nielsen, Numerical simulation of the impact of surgeon posture on airborne particle distribution in a turbulent mixing operating theatre, Build. Environ. 110 (2016) 140–147, http://dx.doi.org/10.1016/j.buildenv.2016.10.005, https://www.sciencedirect.com/science/article/pii/S0360132316303973.

[31] F. Memarzadeh, A.P. Manning, Design and optimization of operating room air distribution systems using computational fluid dynamics modeling, ASHRAE Trans. 127 (1) (2021) 15–27.

[32] A. Agirman, Y.E. Cetin, M. Avci, O. Aydin, Effect of air exhaust location on surgical site particle distribution in an operating room, Build. Simul. 13 (5) (2020) 979–988, http://dx.doi.org/10.1007/s12273-020-0642-1.

[33] A.F. Antoniadis, D. Drikakis, P.S. Farmakis, L. Fu, I. Kokkinakis, X. Nogueira, P.A. Silva, M. Skote, V. Titarev, P. Tsoutsanis, UCNS3D: An open-source high-order finite-volume unstructured CFD solver, Comput. Phys. Comm. 279 (2022) 108453.

[34] T. Potsis, Y. Tominaga, T. Stathopoulos, Computational wind engineering: 30 years of research progress in building structures and environment, J. Wind Eng. Ind. Aerodyn. 234 (2023) 105346, http://dx.doi.org/10.1016/j.jweia.2023.105346, URL https://www.sciencedirect.com/science/article/pii/S0167610523000491.

[35] D.J. Mavriplis, Chapter 7 - mesh generation and adaptivity for complex geometries and flows, in: R. Peyret (Ed.), Handbook of Computational Fluid Mechanics, Academic Press, London, 1996, pp. 417–459, http://dx.doi.org/10.1016/B978-012553010-1/50008-6, https://www.sciencedirect.com/science/article/pii/B9780125530101500086.

[36] R. Kameel, E. Khalil, The prediction of airflow regimes in surgical operating theatres: a comparison of different turbulence models, in: 41st Aerospace Sciences Meeting and Exhibit, 2003, http://dx.doi.org/10.2514/6.2003-859, https://arc.aiaa.org/doi/abs/10.2514/6.2003-859.

[37] S. Mohamed, G. Buonanno, N. Massarotti, M. Mauro, Ultrafine particle transport inside an operating room equipped with turbulent diffusers, J. Build. Perform. Simul. 13 (4) (2020) 443–455, http://dx.doi.org/10.1080/19401493.2020.1766567, https://doi.org/10.1080/19401493.2020.1766567.

[38] K. Goethals, A. Janssens, Sensitivity of the predicted convective heat transfer in a cooled room to the computational fluid dynamics simulation approach, J. Build. Perform. Simul. 6 (6) (2013) 420–436, http://dx.doi.org/10.1080/19401493.2012.737833, https://doi.org/10.1080/19401493.2012.737833.

[39] Y. Tao, K. Inthavong, J. Tu, Computational fluid dynamics study of human-induced wake and particle dispersion in indoor environment, Indoor Built Environ. 26 (2) (2017) 185–198, http://dx.doi.org/10.1177/1420326X16661025, https://doi.org/10.1177/1420326X16661025.

[40] S. Sadrizadeh, A. Tammelin, P. Ekolind, S. Holmberg, Influence of staff number and internal constellation on surgical site infection in an operating room, Particuology 13 (2014) 42–51, http://dx.doi.org/10.1016/j.partic.2013.10.006, https://www.sciencedirect.com/science/article/pii/S167420011300223X.

[41] B. Chaouat, The state of the art of hybrid RANS/LES modeling for the simulation of turbulent flows, Flow Turbul. Combust. 99 (2) (2017) 279–327, http://dx.doi.org/10.1007/s10494-017-9828-8.

[42] S. Heinz, A review of hybrid RANS-LES methods for turbulent flows: concepts and applications, Prog. Aerosp. Sci. 114 (2020) 100597, http://dx.doi.org/10.1016/j.paerosci.2019.100597, https://www.sciencedirect.com/science/article/pii/S0376042119301861.

[43] J. Cho, J. Kim, Y. Kim, Development of a non-contact mobile screening center for infectious diseases: Effects of ventilation improvement on aerosol transmission prevention, Sustainable Cities Soc. 87 (2022) 104232, http://dx.doi.org/10.1016/j.scs.2022.104232.

[44] C. Xu, W. Liu, X. Luo, X. Huang, P.V. Nielsen, Prediction and control of aerosol transmission of SARS-CoV-2 in ventilated context: from source to receptor, Sustainable Cities Soc. 76 (2022) 103416, http://dx.doi.org/10.1016/j.scs.2021.103416.

[45] A. D'Alicandro, A. Mauro, Effects of operating room layout and ventilation system on ultrafine particle transport and deposition, Atmos. Environ. 270 (2022) 118901, http://dx.doi.org/10.1016/j.atmosenv.2021.118901, https://www.sciencedirect.com/science/article/pii/S1352231021007238.

[46] L. Morawska, W. Bahnfleth, P.M. Bluyssen, A. Boerstra, G. Buonanno, S.J. Dancer, A. Floto, F. Franchimon, C. Haworth, J. Hogeling, C. Isaxon, J.L. Jimenez, J. Kurnitski, Y. Li, M. Loomans, G. Marks, L.C. Marr, L. Mazzarella, A.K. Melikov, S. Miller, D.K. Milton, W. Nazaroff, P.V. Nielsen, C. Noakes, J. Peccia, X. Querol, C. Sekhar, O. Seppänen, S.-i. Tanabe, R. Tellier, T.K. Wai, P. Wargocki, A. Wierzbicka, Coronavirus disease 2019 and airborne transmission: Science rejected, lives lost. Can society do better? Clin. Infect. Dis. 76 (10) (2023) 1854–1859, http://dx.doi.org/10.1093/cid/ciad068, arXiv:https://academic.oup.com/cid/article-pdf/76/10/1854/50490599/ciad068.pdf.

[47] F. Romano, L. Marocco, J. Gustén, C.M. Joppolo, Numerical and experimental analysis of airborne particles control in an operating theater, Build. Environ. 89 (1) (2015) 369–379, http://dx.doi.org/10.1016/j.buildenv.2015.03.003, https://www.sciencedirect.com/science/article/pii/S0360132315001067.

[48] R. Knudsen, S. Knudsen, T. Nymark, T. Anstensrud, E. Jensen, M. La Mia Malekzadeh, S. Overgaard, Laminar airflow decreases microbial air contamination compared with turbulent ventilated operating theatres during live total joint arthroplasty: a nationwide survey, J. Hosp. Infect. 113 (2021) 65–70, http://dx.doi.org/10.1016/j.jhin.2021.04.019, URL https://www.sciencedirect.com/science/article/pii/S0195670121001705.

[49] J. Ramirez-Pastran, C. Duque-Daza, On the prediction capabilities of two SGS models for large-eddy simulations of turbulent incompressible wall-bounded flows in OpenFOAM, in: D. Pham (Ed.), Cogent Eng. 6 (1) (2019) 1679067, http://dx.doi.org/10.1080/23311916.2019.1679067, URL https://www.tandfonline.com/doi/abs/10.1080/23311916.2019.1679067. arXiv:https://www.tandfonline.com/doi/pdf/10.1080/23311916.2019.1679067.

[50] E.L. Kermani, E. Roohi, F. Porté-Agel, Evaluating the modulated gradient model in large eddy simulation of channel flow with OpenFOAM, J. Turbul. 19 (7) (2018) 600–620, http://dx.doi.org/10.1080/14685248.2018.1483078, arXiv:https://doi.org/10.1080/14685248.2018.1483078.

[51] E. Komen, A. Shams, L. Camilo, B. Koren, Quasi-DNS capabilities of OpenFOAM for different mesh types, Comput. & Fluids 96 (2014) 87–104, http://dx.doi.org/10.1016/j.compfluid.2014.02.013, URL https://www.sciencedirect.com/science/article/pii/S0045793014000760.

[52] Y. Addad, I. Zaidi, D. Laurence, Quasi-dns of natural convection flow in a cylindrical annuli with an optimal polyhedral mesh refinement, Comput. & Fluids 118 (2015) 44–52, http://dx.doi.org/10.1016/j.compfluid.2015.06.014, URL https://www.sciencedirect.com/science/article/pii/S0045793015001978.

[53] G. Lecrivain, R. Rayan, A. Hurtado, U. Hampel, Using quasi-DNS to investigate the deposition of elongated aerosol particles in a wavy channel flow, Comput. & Fluids 124 (2016) 78–85.

[54] E. Komen, L.H. Camilo, A. Shams, B.J. Geurts, B. Koren, A quantification method for numerical dissipation in quasi-DNS and under-resolved DNS, and effects of numerical dissipation in quasi-DNS and under-resolved DNS of turbulent channel flows, J. Comput. Phys. 345 (2017) 565–595.
[55] F. Cadieux, G. Sun, J.A. Domaradzki, Effects of numerical dissipation on the interpretation of simulation results in computational fluid dynamics, Comput. & Fluids 154 (2017) 256–272.
[56] S.B. Pope, Turbulent flows, Meas. Sci. Technol. 12 (11) (2001) 2020–2021.
[57] M. Germano, U. Piomelli, P. Moin, W.H. Cabot, A dynamic subgrid-scale eddy viscosity model, Phys. Fluids A: Fluid Dyn. 3 (7) (1991) 1760–1765.
[58] A.C. García, A.C. Rodríguez, K.T.N. Buñay, A.M.L. Aleaga, L.L. Lorente-Leyva, Pineapple drying analysis in packing plants through computational fluid dynamics, Int. J. Des. Nat. Ecodyn. 17 (1) (2022) 29–35, http://dx.doi.org/10.18280/ijdne.170104.
[59] I.B. Celik, U. Ghia, P.J. Roache, C.J. Freitas, Procedure for estimation and reporting of uncertainty due to discretization in CFD applications, J. Fluids Eng.-Trans. ASME 130 (7) (2008).
[60] A. Moreno-Rangel, F. Musau, T. Sharpe, G. McGill, Indoor air quality assessment of Latin America's first Passivhaus home, Atmosphere 12 (11) (2021) 1477.
[61] K.-C. Chung, S.-P. Hsu, Effect of ventilation pattern on room air and contaminant distribution, Build. Environ. 36 (9) (2001) 989–998.
[62] Y.-L. Wu, Y.-L. Wu, A.H. Hanifan, Study on ventilation performance in operating room with variation ventilation design, in: Journal of Physics: Conference Series, Vol. 1500, IOP Publishing, 2020, 012040.
[63] M. Regard, F. Carrie, A. Voeltzel, V. Richalet, Measurement and CFD modeling of IAQ indices, in: Proc. of 16th AIVC Conference, 1995.
[64] T. Nakai, M. Van Der Molen, J. Gash, Y. Kodama, Correction of sonic anemometer angle of attack errors, Agricult. Forest Meteorol. 136 (1–2) (2006) 19–30.
[65] M. Aubinet, T. Vesala, D. Papale, Eddy Covariance: a Practical Guide to Measurement and Data Analysis, Springer Science & Business Media, 2012.
[66] A. Peña, E. Dellwik, J. Mann, A method to assess the accuracy of sonic anemometer measurements, Atmos. Meas. Tech. 12 (1) (2019) 237–252.
[67] A. Dyer, Flow distortion by supporting structures, Bound.-Lay. Meteorol. 20 (2) (1981) 243–251.
[68] U. Högström, A.-S. Smedman, Accuracy of sonic anemometers: laminar wind-tunnel calibrations compared to atmospheric in situ calibrations against a reference instrument, Bound.-Layer Meteorol. 111 (2004) 33–54.
[69] J. Kochendorfer, T.P. Meyers, J. Frank, W.J. Massman, M.W. Heuer, How well can we measure the vertical wind speed? Implications for fluxes of energy and mass, Bound.-Layer Meteorol. 145 (2012) 383–398.
[70] T. Nakai, K. Shimoyama, Ultrasonic anemometer angle of attack errors under turbulent conditions, Agricult. Forest Meterol. 162 (2012) 14–26.
[71] T. Derrick, J. Thomas, Time series analysis: the cross-correlation function, 2004.
[72] R.D. Keane, R.J. Adrian, Theory of cross-correlation analysis of PIV images, Appl. Sci. Res. 49 (1992) 191–215.
[73] A. Brito, F.R. Santos, A. de Castro, A. da Cunha Lima, G. Zebende, I. da Cunha Lima, Cross-correlation in a turbulent flow: Analysis of the velocity field using the ρdcca coefficient, Europhys. Lett. 123 (2) (2018) 20011.
[74] R. American Society of Heating, A.-C. Engineers, ASHRAE Standard: Ventilation for Acceptable Indoor Air Quality, ASHRAE, 2019.
[75] S.A. Kalantari, S.V. Patankar, Evaluation of HVAC design parameters in high-performance hospital operating theatres, Sustainability 13 (4) (2021) 2043, URL https://www.mdpi.com/2071-1050/13/4/2043/pdf.
[76] M. Henriksson, H. Nilsson, Ventilation Efficiency Measurements-A Comparison Between Three Supply Air Methods, Lund University, 2016.